Enhancer-based AAV approach for selective AADC delivery reduces motor symptoms and dyskinesia in Parkinson's mouse models

Ananya Chowdhury[1*], Alex Fraser[1*], Max Departee[1], Naz Taskin[1], Meagan A. Quinlan[1], John K. Mich[1], Victoria Omstead[1], Nathaly Lerma[1], Ximena Opitz-Araya[1], Alex C. Hughes[1], Emily Kussick[1], Refugio Martinez[1], Melissa Reding[1], Elizabeth Liang[1], Lyudmila Shulga[1], Dean Rette[1], Cindy Huang[1], Brittny Casian[1], Madison Leibly[1], Olivia Helback[1], Tyler Barcelli[1], Toren Wood[1], Nicholas Uribe[1], Colin Bacon[1], Jessica Bowlus[1], Dakota Newman[1], Rana Kutsal[1], Shannon Khem[1], Nicholas Donadio[1], Shenqin Yao[1], Kara Ronellenfitch[1], Vonn Wright[1], Kathryn Gudsnuk[1], Greg D. Horwitz[3], Boaz P. Levi[1], Ed S. Lein[1], Jonathan T. Ting[1,2,3], Tanya L. Daigle[1,3**]

Author Affiliations and Footnotes:

[1] Allen Institute for Brain Science, Seattle, WA 98109, USA.

[2] Washington National Primate Research Center, Seattle, WA 98195 USA.

[3] Department of Neurobiology and Biophysics, University of Washington, Seattle, WA 98195 USA.

*Contributed equally

**Corresponding Author

Correspondence: Tanya L. Daigle, tanyad@alleninstitute.org

Keywords

AAV, AADC, neurodegeneration, Parkinson's disease, therapy, L-DOPA, striatum, dopamine, nigrostriatal, motor behaviors, locus coeruleus

Summary

Profound degeneration of dopamine (DA) neurons and reduced DA levels in the brain is recognized as an underlying cause of Parkinson's Disease (PD). The standard treatment for PD

is levodopa (L-DOPA), but its effectiveness wanes over time and prolonged usage can lead to L-DOPA-induced-dyskinesia (LID). An adeno-associated virus (AAV)-based strategy to overexpress aromatic l-amino acid decarboxylase (AADC) in the striatum combined with L-DOPA therapy shows promise for symptomatic improvement but requires an invasive delivery approach. Here, we generated enhancer AAVs to drive AADC expression in key cell types and paired them with a blood-brain barrier (BBB)-penetrant capsid. We characterized the AAVs in mouse following multiple routes of administration and found that cell-type specific viral treatment ameliorated motor deficits and LID in PD disease models. This cell type-specific viral rescue strategy showed similar or better phenotypic rescue compared to a ubiquitous targeting approach and improved mortality. Additionally, we characterized the expression of an AAV-AADC vector capable of mouse phenotypic rescue in non-human primate (NHP) following two routes of administration. This novel therapeutic strategy in combination with L-DOPA may enable a less invasive and better tolerated approach to treat motor deficits in PD patients.

Introduction

Parkinson's disease (PD) is a progressive neurodegenerative disease that afflicts more than 10 million people worldwide[1,2] and is characterized by severe motor symptoms ranging from rigidity, tremors, and gait imbalance to grip difficulty, speech deficits, and micrographia.[3,4] Though selective loss of midbrain dopaminergic cells and depletion of striatal dopamine (DA) has been recognized as one of the underlying neuropathology of PD,[5–7] there is still no cure or therapeutics that slow the disease progression. The most widely used treatment is administration of the DA precursor, levodopa (L-DOPA). While beneficial in the short-term, prolonged L-DOPA use causes debilitating motor dyskinesias (i.e., impairments in regular movements), collectively called LID (L-DOPA-induced dyskinesia).[8–11] Because LID negatively impacts patients' quality of life and increases economic burden on their families,[1,2] the

development of a new therapeutic approaches to provide relief from the motor symptoms of PD with fewer side-effects are needed.

Gene therapy has the potential to provide long-term clinical benefits.[12,13] In the last decade, advancements in genetic modifications, viral vectors, and precision surgery have allowed a rapid surge of clinical trials focused on gene delivery to treat neurological diseases.[14–18] For dopamine-deficient disorders, particularly promising results were obtained from trials that used adeno-associated virus 2 (AAV2) to drive the expression of human aromatic l-amino acid decarboxylase (AADC), a key enzyme in DA synthesis.[19] These results led to European Medicines Agency (EMA) and U.S. Food and Drug Administration (FDA) to approve this approach as a treatment for AADC deficiency in children.[20–22] An AAV2-AADC delivered under the control of a ubiquitous, cytomegalovirus (CMV) promoter in combination with L-DOPA has been extensively tested in the context of PD and has been shown to augment brain dopamine levels and improve motor outcomes in rodents and non-human primates.[23–28] Additionally, the AAV2-AADC gene therapy approach was shown to be well tolerated in human patients but it requires bilateral and direct putaminal infusion, which is highly invasive, not scalable, and prone to technical issues.[29–32]

Non-invasive routes of administration, like the intravenous (IV) delivery of the commercially available blood-brain barrier (BBB)-penetrant capsid,[33] have shown great promise in the pre-clinical studies[34] and have recently been approved for clinical trials for GBA1-PD therapy.[35] Additionally, considerable progress has been made in the AAV capsid engineering space and emerging BBB penetrant capsids like BI-hTFR1[36] and VCAP-102[37] may soon enable systemic gene therapies for central nervous system (CNS) disorders. Achieving this goal will likely require precision targeting across cell type, organ, and systemic levels to minimize off-target toxicity and lethality, thereby precluding the use of ubiquitous promoter strategies.[34,38]

We have developed an enhancer-based AAV platform capable of achieving robust and cell type-specific transgene expression across diverse neuronal and non-neuronal populations in the

CNS via both direct and systemic delivery routes.[39–43] Furthermore, we recently have shown that an enhancer-driven or cell type-promoter based AAV strategy can be effective for correcting major circuit-level defects in severe neurodevelopmental disorders.[44,45] These advances underscore the broad therapeutic potential of cell type-selective gene delivery strategies for a range of neurological disorders, with PD representing a promising target yet to be investigated. Here, we generated enhancer-driven AAVs to drive expression of human AADC in select striatal and dopaminergic cell types. Extensive characterization of each vector in mice following different routes of administration revealed a novel AADC expression pattern in the brain. We then evaluated the efficacy of a medium spiny neuron (MSN)-enhancer driven AADC-AAV delivered in combination with L-DOPA and found reversal of select motor deficits in both 6-hydroxydopamine (6-OHDA) and MCI-Park PD mouse models. The extent of MSN-AADC-AAV phenotypic rescue was found to be comparable or better than the ubiquitous promoter-driven AADC vector, and additionally cell type-specific treatment reduced LID in the 6-OHDA model. We further tested the efficacy of AADC-AAV targeting striatal cholinergic, dopaminergic, and non-neuronal populations and found selective rescue of motor deficits only in the rapid model, but not the progressive PD model. Lastly, we evaluated expression of the MSN-AADC-AAV in NHP following clinically relevant routes of administration and found preserved specificity within the caudate and putamen. In summary, these data provide strong proof-of-concept in support of enhancers-AAVs in combination with L-DOPA as a potential therapy for motor symptoms in PD, which could potentially be delivered non-invasively with a BBB-penetrant capsid.

Results

Development and validation of cell-type selective AADC expressing AAVs

To determine if selective expression of AADC within MSNs could be beneficial for the treatment of motor symptoms in PD, we developed enhancer-containing viral vectors capable of delivering AADC to the relevant cell type in the striatum. An MSN enhancer (AiE0450h) was previously

shown to drive selective expression of the fluorescent SYFP2 reporter in the mouse when placed upstream of a minimal β-globin promoter[40] (AiE0450h-SYFP2; AiP12236; **Figure 1A, left panel**). To selectively drive AADC expression, we replaced SYFP2 with a codon-optimized human *DDC* gene (AiE0450h-AADC(no intron)-HA; AiP16390; **Figure S1A, left panel**). In addition, we generated three variants that incorporated the following introns: human hemoglobin β third intron (HBB3)[44] (AiE0450h-AADC(HBB3)-HA; AiP13663; **Figure 1A, middle panel**), SV40 small-t intron[46] (AiE0450h-AADC(SV40 small-t)-HA; AiP16391; **Figure S1A, middle panel**), and a longer SV40 intronic sequence[47] (AiE0450h-AADC(SV40)-HA; AiP16392; **Figure S1A**, **right panel**). A C-terminal 3xHA epitope tag was added in all vectors for immunochemical detection of AADC. The viral constructs were packaged in the BBB-penetrant PHP.eB capsid[33] and injected retro-orbitally (RO) into adult wild-type C57BL6/J mice at 1e12 viral genomes (vg) per animal. 3 weeks post injection, fixed brains were collected and analyzed for AADC expression in the striatum, revealed with an anti-HA epitope. The intronless construct and SV40 small-t intron construct showed no detectable expression and the longer SV40 intron supported very weak expression (**Figure S1B**). In contrast, the HBB3 intron drove robust transgene expression (AADC-HA), consistent with the enhancer activity previously observed with SYFP2[40] (**Figure 1D, middle panel**). Based on their striatal expression, we selected the AADC-HA design with HBB3 intron for further validation (henceforth referred to as AiE0450h-AADC-HA for simplicity). Furthermore, we generated a version in which the identical *DDC* gene sequence was driven by the ubiquitous CMV promoter, same as the clinical candidate AAV-AADC vector,[29–31] and added the HBB3 intron and 3xHA epitope tag (CMV-AADC-HA; AiP16328, **Figure 1A, right panel**) to make it comparable to the enhancer-AAV-AADC.

The expression profiles of AiE0450h-SYFP2, AiE0450h-AADC-HA, and CMV-AADC-HA were then tested via immunohistochemical detection of the respective transgenes. SYFP2 expression was restricted to the MSNs in the striatum (STR) with visible viral tracts that extended to the ventral tegmental area and substantia nigra (VTA/SN) as expected[40] (**Figure 1B; left panel**).

AiE0450h-AADC-HA showed robust striatal localization as well as substantial expression of the transgene-driven HA in the VTA/SNc and LC (**Figure 1B; middle panel**). These brain regions have been known to endogenously express the *Ddc* gene, as confirmed by in situ hybridization (ISH) data from the mouse Allen Brain Atlas (**Figure 1C**). Testing of CMV-AADC-HA vector revealed transgene expression throughout the brain, including within the VTA/SNc and LC (**Figure 1B, right panel**), consistent with the ubiquitous nature of the CMV promoter.

Next, we assessed whether AiE0450h-AADC-HA targeted MSNs in the striatum by co-staining fixed brain sections with the antibodies against the HA epitope and DARPP-32, an MSN marker.[48] As expected, AiE0450h-driven AADC-HA expression showed strong overlap with DARPP-32+ MSNs in the striatum, similar to native SYFP2 signal in AiE0450h-SYFP2 (white arrows, **Figure 1D, left and middle panels**). In contrast, CMV-driven AADC-HA expression was found in multiple other neuronal and non-neuronal populations, in addition to DARPP-32+ MSNs (**Figure 1D, right panel**).

Since we observed AADC-HA expression in extra-striatal regions, including in the VTA/SNc and LC, we further examined co-localization of AADC-HA with the catecholaminergic marker tyrosine hydroxylase (TH).[49,50] In contrast to the SYFP2-expressing control in the corresponding areas (**Figure 1E-F, left panels**), both AiE0450h-driven and CMV-driven AADC-HA showed robust co-localization with TH+ neurons in VTA (white arrows**, Figure 1E, middle and right panels;** completeness**:** 63.33 ± 4.23 % for AiE0450h and 41.07 ± 2.04 % for CMV, specificity: 67.08 ± 1.95 % for AiE0450h and 73.69 ± 0.38 % for CMV) and SNc (completeness: 81.86 ± 2.57 % for AiE0450h and 67.49 ± 5.44 % for CMV, specificity: 75.53 ± 3.40 % for AiE0450h and 57.96 ± 6.32 % for CMV). Similarly, strong co-labeling was also observed in LC (white arrows, **Figure 1F, middle and right panels;** completeness: 77.71 ± 3.30 % for AiE0450h and 41.81 ± 3.54 % for CMV, specificity: 63.74 ± 2.83 % for AiE0450h and 48.13 ± 2.40 % for CMV), indicating AADC-HA transgene expression in the catecholaminergic neurons. Compared to the CMV-driven AADC-HA, AiE0450h-AADC-HA showed significantly higher completeness in the TH+

neurons in VTA (p= 0.006) and LC (p <0.0001) with comparable specificity in all three areas (**Figure S5A-B**). Similar to their lack of efficacy in the striatum, both the intronless and the longer SV40 constructs produced no detectable or very weak expression in VTA/SNc or LC, whereas the SV40 small-t intron construct resulted in minimal expression in both areas **(Figure S1C-D)**, which may suggest this extrastriatal expression could be an inherent feature of the transgene and not the precise vector design.

To quantitatively compare expression levels in the striatum, virally expressed HA epitope and total AADC protein were measured by Western blot. For both AiE0450h-AADC-HA and CMV-AADC-HA, HA and viral AADC signals were detected at the same molecular weight as expected, with the viral AADC band having a slightly higher molecular weight than endogenous AADC (**Figure 1G**), consistent with the added 3xHA tag. Comparison of protein levels revealed that the CMV promoter drove 8.66 ± 0.64-fold higher levels of AADC-HA than the AiE0450h-AADC-HA vector did (**Figure 1H**). The strong transgene expression produced by CMV-AADC-HA exceeded physiological levels, reaching 693.0 ± 53.8 % the amount of endogenous protein (**Figure 1I**). In contrast, AiE0450h-AADC-HA yielded 40.3 ± 14.3 % the amount of endogenous AADC (**Figure 1I**). We also examined a non-striatal area (M1 cortex) and found that both HA and AADC transgene bands were detected only in CMV-AADC-HA–injected animals, with no detectable signal for AiE0450h-AADC-HA or control animals (data not shown).

Together, these findings confirmed that RO delivery of AiE0450-ehancer driven AADC maintains selective expression in MSNs while also revealing pronounced extrastratial expression in Ddc-positive regions, including the VTA/SNc and LC. As expected, the CMV promoter drove significantly higher transgene expression in all three regions analyzed and had a broader brain-wide distribution.

Retro-orbital administration of AiE0450h-AADC-HA rescued specific motor behaviors in 6-OHDA unilateral toxin model

To investigate the therapeutic potential of RO delivery of AAV-AADC into the brain, we used an established unilateral toxin mouse model of PD. Adult wild-type C57Bl6/J mice received a unilateral stereotaxic injection of 6-hydroxydopamine (6-OHDA)[51–53] into the dorsal striatum to generate a rapid dopamine-depletion model. The retrogradely transported toxin resulted in severe degeneration of TH+ fibers at the injection site and loss of TH+ dopamine neurons in the VTA (45.37 ± 7.03 %) and SNc (85.55 ± 4.97 %) in the injected hemisphere compared to the intact side (**Figure S2A**).

The toxin-lesioned mice were RO injected with either vehicle, AiE0450h-SYFP2, CMV-AADC-HA, or AiE0450h-AADC-HA at 1e12 vg dose, followed by phenotypic observation and behavioral testing 3 weeks later (**Figure 2A**). To evaluate the efficacy of virally mediated AADC expression in rescuing PD-related motor symptoms, we performed three behavioral paradigms: accelerating rotarod to test motor coordination, open field to check exploratory behavior, and cylinder test to examine forelimb asymmetry (**Figure 2B-C**).

Consistent with the model, toxin treatment alone caused a significant reduction in the latency to fall in the accelerating rotarod (no toxin control: 180.42 ± 11.97 s, toxin only control: 106.71 ± 11.06 s; p=0.0012; **Figure 2B, left panel**), total distance traveled in the open field (no toxin control: 9911.56 ± 709.57 cm, toxin only control: 7413.06 ± 507.49 cm; p=0.008; **Figure 2B, middle panel**), and percentage of contralateral paw touches for supported rearing in the cylinder (no toxin control: 24.49 ± 2.12 %, toxin only control: 13.43 ± 1.91%; p=0.001; **Figure 2B, right panel**). In the absence of its substrate, L-DOPA, RO delivery of AADC-HA, either driven by CMV-promoter or AiE0450h-enhancer, failed to rescue the motor phenotypes of the toxin-lesioned mice (**Figure 2B**). Compared to the toxin only control, without L-DOPA, the virally treated mice did not improve in their latency to fall in the accelerating rotarod (CMV-AADC-HA: 114.13 ± 18.90 s, AiE0450h-AADC-HA: 132.79 ± 7.85 s; **Figure 2B, left panel**), total distance travelled in the open field (CMV-AADC-HA: 8485.05 ± 498.16 cm, AiE0450h-AADC-HA: 7868.74 ± 405.92 cm; **Figure 2B, middle panel**), and percentage of contralateral paw touches for

supported rearing in the cylinder (CMV-AADC-HA: 12.03 ± 2.15 %, AiE0450h-AADC-HA: 18.51 ± 1.44 %; **Figure 2B, right panel**).

As expected, the viral treatment in the absence of L-DOPA failed to rescue the motor deficits. Therefore, we next tested a subthreshold dose of L-DOPA combined with viral AADC expression and determined the amount of L-DOPA that would fail to rescue the toxin-induced impairment itself. To that effect, a low dose of L-DOPA (1.5 mg/kg) was intraperitoneally administered to the toxin-lesioned mice, and their behavioral phenotype was evaluated 45 minutes later. Compared to the toxin only control, at this dose, the L-DOPA-treated animals (no virus control) showed no improvement in the latency to fall in the accelerating rotarod (toxin only control: 76.41 ± 6.60 s, no virus control: 104.07 ± 8.85 s; **Figure 2C, left panel**), distance travelled in the open field (toxin only control: 7780.27 ± 243.31 cm, no virus control: 9036.22 ± 517.94 cm; **Figure 2C, middle panel**), and percentage of contralateral paw touches in the cylinder (toxin only control: 11.19 ± 1.52 %, no virus control: 15.95 ± 2.92 %; **Figure 2C, right panel**).

When 1.5 mg/kg of L-DOPA was administered to the toxin-lesioned mice that received AiE0450h-AADC-HA, the animals significantly increased the time spent on the accelerating rotarod compared to the other virally treated conditions (AiE0450h-AADC-HA: 168.82 ± 6.08 s, AiE0450h-SYFP2: 90.48 ± 8.49 s, CMV-AADC-HA: 84.52 ± 8.54 s) and the controls stated above ($p < 0.0001$ for all; **Figure 2C, left panel**). Additionally, AiE0450h-AADC-HA treated mice exhibited significantly higher use of their contralateral paw while rearing in the cylinder compared to AiE0450h-SYFP2 (AiE0450h-AADC-HA: 25.42 ± 2.71 %, AiE0450h-SYFP2: 15.85 ± 2.37 %; $p=0.0260$), toxin only control ($p=0.0002$) and no virus control ($p=0.0419$; **Figure 2C, right panel**). In contrast, AiE0450h-AADC-HA treated animals did not significantly increase their distance travelled in the open field than the AiE0450h-SYFP2 mice (AiE0450h-AADC-HA: 8734.77 ± 365.90 cm, AiE0450h-SYFP2: 7613.45 ± 292.24 cm) or the aforementioned controls, but they performed significantly better than CMV-AADC-HA cohort (6747.60 ± 566.09 cm,

p=0.0057; **Figure 2C, middle panel**). RO administration of CMV-AADC-HA could not be tested for contralateral paw touches in the cylinder due to the failure of the injected animals to rear. Additionally, the toxin-lesioned mice that received AiE0450h-AADC-HA had a lower mortality rate (12.5% of total injected) than those that received CMV-AADC-HA (62.5% of total injected; **Figure S2B**), indicating the widespread expression of AADC under the CMV promoter further exacerbates their condition. Furthermore, since the unilateral lesion model provides the opportunity to study dopaminergic imbalance between the lesioned and intact sides,[23,54,55] we examined motor asymmetry as a phenotype for the effect of AADC delivery to mice. The AiE0450h-AADC-HA cohort showed no occurrences of dragging their contralateral hindlimbs and contralateral rotations (collectively called contralateral movements) over 10 mins in a cylinder while those that received CMV-AADC-HA exhibited significant contralateral movements (number of occurrences: 12.50 ± 3.97, time spent: 65.72 ± 26.56 s; p=0.0046; **Figure S2C**). Collectively, these data demonstrate strong phenotypic rescue of select motor deficits with RO delivery of cell type-selective viral AADC-HA that is on par with or better than the leading clinical candidate vector. Additionally, the cell type-selective approach reduced mortality and exhibited no detectable contralateral movements, which suggests improved tolerability at whole body level.

Intra-striatal administration of AiE0450h-AADC-HA and CMV-AADC-HA rescued specific motor behaviors in 6-OHDA unilateral toxin model

To directly compare viral efficacy with the route of administration being used in current clinical trials,[29–31] we injected 1e9 vg of each vector bilaterally into the dorsal striatum of the mice. 3 weeks later, we perfused the mice and analyzed the brain immunohistochemically for specificity and completeness of viral transduction.

Both AiE0450h-AADC-HA and CMV-AADC-HA showed comparable spread and robust expression of the transgene-driven HA within the striatum **(Figure 3A).** Western blot analysis revealed increased levels of HA expression with CMV-AADC-HA, averaging 3.32 ± 1.35-fold

expression relative to AiE0450h-AADC-HA following intra-striatal injection (**Figure 3D-E**). Consistently, CMV-AADC-HA drove viral AADC expression to 1623 ± 683 % above endogenous AADC, whereas AiE0450h-AADC-HA resulted in a 306 ± 54% increase (**Figure 3F**).

However, at the injected dose of 1e9 vg per hemisphere, intra-striatal administration of the vectors (**Figure 3B-C**) showed significantly reduced AADC-HA completeness in the TH+ neurons of VTA (2.19 ± 0.51 % for AiE0450h and 8.80 ± 1.77 % for CMV), SNc (0.83 ± 0.44 % for AiE0450h and 9.04 ± 2.53 % for CMV), and LC (0.76 ± 0.41 % for AiE0450h and 1.53 ± 0.56 % for CMV) compared to their RO injected counterparts (**Figures 1D-F and S5B**; $p<0.0001$ for all three areas with both viruses). Despite their diminished expression in the extrastriatal regions, compared to the RO injection of the respective vectors, the intra-striatal administration did not significantly reduce the specificity of AADC-HA expression within the TH+ neurons of VTA (33.31 ± 6.57 % for AiE0450h and 58.09 ± 5.49 % for CMV) and LC (40.74 ± 21.89 % for AiE0450h and 43.80 ± 4.38 % for CMV). However, in the TH+ neurons of SNc, intra-striatal delivery of AiE0450h-AADC-HA resulted in significantly lower specificity (22.22 ± 11.11 %) compared to RO of the same vector ($p= 0.0016$) and intra-striatal administration of CMV-AADC-HA (70.42 ± 2.52 %, $p= 0.0050$; **Figure S5B**). Increasing the viral load of AiE0450h-AADC-HA to 1e10 vg per hemisphere resulted in a comparatively higher expression of AADC-HA expression in VTA (completeness: 18.51%, specificity: 50.71%), SNc (completeness: 27.04%, specificity: 69.16%), and LC (completeness: 6.04%, specificity: 56.81%) but remained qualitatively lower than RO delivery of the same virus (**Figures S3 and S5A**)**.** Together, these data demonstrates that intra-striatal administration promotes strong AADC expression in striatal MSNs, but in contrast to RO injection, extrastriatal expression is significantly reduced.

To assess the therapeutic potential of direct viral AADC delivery, next we performed bilateral intra-striatal surgeries to administer 1e9 vg of these viral vectors to the unilaterally toxin-lesioned mice and evaluated them in behavioral paradigms with the aforementioned low L-DOPA dose (1.5mg/kg, i.p) 3 weeks later (**Figure 3G**)**.** Delivering AiE0450h-AADC-HA into the

striatum of the toxin-lesioned mice increased their time spent on the accelerating rotarod (165.17 ± 9.94 s) which was on par with the CMV-AADC-HA-treated, toxin-lesioned mice (161.02 ± 9.38 s; p=0.9997; **Figure 3H, left panel**). Both the AADC-HA vectors showed significant improvement in the accelerating rotarod compared to the toxin-lesioned controls (Toxin only control: 81.05 ± 9.85 s, p<0.0001 for both vectors; No virus control: 112.61 ± 10.98 s, p=0.0083 (AiE0450h-AADC-HA), p=0.0190 (CMV-AADC-HA); AiE0450h-SYFP2: 117.33 ± 11.66 s, p =0.0429 (AiE0450h-AADC-HA; **Figure 3H, left panel**). Similarly, the percentage of contralateral paw touches used for supported rearing in the cylinder was comparable between the AiE0450h-AADC-HA animals (18.61 ± 2.34 %) and those that received CMV-AADC-HA (16.36 ± 1.85 %; p=0.9121; **Figure 3H, right panel**). Both AADC-HA treated mice exhibited higher use of contralateral paw than the toxin only control (8.04 ± 0.97 %, p= 0.0007 (AiE0450h-AADC-HA), p= 0.0138 (CMV-AADC-HA)) but not when compared to no virus controls (13.74 ± 1.61 %) and AiE0450h-SYFP2-treated mice (12.62 ± 1.67 %; **Figure 3H, right panel**). However, this treatment strategy did not ameliorate their voluntary, gross motor movement deficit in the open field (Toxin only control: 8188.89 ± 311.71 cm, No virus control: 8229.60 ± 476.50 cm, AiE0450h-SYFP2: 7994.12 ± 417.35 cm, CMV-AADC-HA: 8655.78 ± 427.24 cm, AiE0450h-AADC-HA: 8014.09 ± 356.57 cm**; Figure 3H, middle panel**). Intra-striatal administration of AADC-HA did not cause increased mortality or worsening of phenotype in the toxin-lesioned mice for both vectors (data not shown).

Together, these experiments confirmed that consistent with systemic delivery, more targeted administration of the cell type-specific virus yielded similar improvements in the same behavioral tests. Additionally, the enhancer-driven AADC-HA rescued PD-related motor symptoms as efficiently as the CMV-promoter vector with direct delivery of the therapeutic cargo into the striatum.

Intra-striatal administration of AiE0450h-AADC-HA reduced L-DOPA-induced dyskinesia (LID) in 6-OHDA unilateral toxin model

Despite L-DOPA being the commonly used treatment for PD, protracted drug administration oftentimes results in the development of abnormal, involuntary movements (AIMs) of the face, extremities and trunk, collectively referred to as L-DOPA-induced dyskinesia (LID).[8,56–59] To determine the dose of L-DOPA best suited to study LID in the toxin-lesioned mice, we performed a dose-behavioral response curve with a single intraperitoneal injection of L-DOPA as before (**Figure 4A**)**.** When normalized to the toxin-lesioned mice that received saline (0.00 ± 8.90 %), the 3 mg/kg dose (48.76 ± 10.46 %; p=0.0174), 5 mg/kg dose (61.64 ± 7.76 %; p= 0.0017), and 10 mg/kg dose (36.44 ± 12.68 %; p=0.0490) of L-DOPA showed significant improvement in the time spent on the accelerating rotarod (**Figure 4B, left panel**). The distance travelled in the open field increased significantly at 3 mg/kg (25.82 ± 7.31 %; p=0.0339) and 5 mg/kg (29.47 ± 7.03 %; p=0.0119) doses when normalized to the saline-treated mice (0.0 ± 4.79 %; **Figure 4B, middle panel**). Both low (1.5 mg/kg) and high (20 mg/kg) L-DOPA doses failed to rescue the motor deficits in the toxin-lesioned mice in the accelerating rotarod (1.5 mg/kg: 33.63 ± 14.88 %, 20 mg/kg: 33.65 ± 3.96 %) and in the open field (1.5 mg/kg: 18.50 ± 8.63 %, 20mg/kg: -3.80 ± 11.99 %**; Figure 4B, left and middle panels**)**.** Furthermore, as expected from the unilateral toxin model, increasing the L-DOPA doses also resulted in significantly higher net contralateral rotations over 10 min in the mice due to hypersensitivity of the DA receptors in the lesioned side[60] (5 mg/kg: 87.38 ± 23.17, p=0.0023; 10 mg/kg: 81.50 ± 22.93, p=0.0044; 20 mg/kg: 140.75 ± 29.63, p <0.0001) while the lower doses exhibited comparably less net turns (1.5 mg/kg: -9.00 ± 3.06, 3 mg/kg: 7.5 ± 3.46) compared to saline controls (-9.38 ± 3.38**; Figure 4B, right panel**). Since a single injection of 5 mg/kg of L-DOPA showed both strong rescue in motor behaviors and induced contralateral rotations in the mice, we proceeded to test the effect of long-term administration of this dose in presence of virally delivered AADC. 3 weeks after unilateral 6-OHDA lesioning, the mice received bilateral injections of 1e9 vg per hemisphere of the vectors, followed by daily L-DOPA injections (5mg/kg, i.p) for 2 weeks (**Figure 4C**). We scored the dyskinetic AIMs affecting the axial, limb, and orolingual (ALO) muscles of the toxin-lesioned

mice over a 10 min duration in the cylinder on the final day, 45 mins after the L-DOPA injection. The cumulative AIMs occurrence increased significantly in mice that received L-DOPA for 2 weeks without virus treatment (17.31 ± 2.40) compared to those that received saline for the same number of days, either without virus (2.46 ± 0.55, $p < 0.0001$), or after intra-striatal injection of AiE0450h-AADC-HA (2.00 ± 0.37, $p < 0.0001$). When treated with the same regimen of L-DOPA, significant reduction of AIMs was observed in mice that received intra-striatal bilateral delivery of AiE0450h-AADC-HA (10.38 ± 1.47, p=0.0093) but not in the CMV-AADC-HA mice (15.57 ± 1.88, p=0.9162), though there was no significant difference between the two vectors (**Figure 4D, left panel**). This longer regimen of 5 mg/kg L-DOPA significantly increased the net contralateral rotations (50.62 ± 9.73, $p < 0.0001$) compared to the saline controls (no virus: -12.77 ± 3.54, AiE0450h-AADC-HA: -13.50 ± 1.95), as was previously observed with the single injection. As before, this rotational phenotype was also significantly alleviated by bilateral administration of AiE0450h-AADC-HA (21.62 ± 4.54, p=0.0088) but not with CMV-AADC-HA (29.43 ± 10.70, p=0.1776; **Figure 4D, right panel**).

These data strongly suggest that cell-type specific AADC treatment in the brain could be sufficient in reducing the harmful impact of long-term L-DOPA treatment.

AiE0450h-AADC-HA rescued specific motor behaviors in MCI-Park genetic model

To determine if the selective viral AADC expression could be beneficial in a progressive mouse model of PD, we next used a genetic model where the gene encoding an essential subunit of the MCI catalytic core, *Ndufs2*, had been selectively deleted from dopaminergic neurons in the brain.[61] Floxed *Ndufs2* mice (*Ndufs2*$^{fl/fl}$) were crossed with mice expressing Cre recombinase (Cre) under the control of the DA transporter (DAT, encoded by *Slc6a3*) promoter (*Slc6a3*$^{+/cre}$) to generate the conditional *Ndufs2*-knockouts (*Slc6a3*$^{+/cre}$; *Ndufs2*$^{fl/fl}$; henceforth referred to as MCI-Park mice). Their littermates expressing floxed *Ndufs2* in the absence of Cre recombinase (*Slc6a3*$^{+/+}$; *Ndufs2*$^{fl/fl}$) were used as age-matched controls (henceforth referred to as controls). Consistent with previous findings,[61] we detected a profound, bilateral depletion of TH+ axonal

projections in the dorsal striatum and cell loss in the VTA/SNc of the MCI-Park mice at P60 (**Figure S4A**).

Since the loss of TH+ axonal staining can already be observed in the dorsal striatum from P30,[61] we chose P30-35 as the age for the MCI-Park mice to receive RO injection of either vehicle (no virus control), AiE0450h-SYFP2, CMV-AADC-HA, or AiE0450h-AADC-HA viruses at 1e12 vg dose each. 4 weeks later, around P58-63, the behavior of these mice was evaluated in different paradigms (**Figure 5A and D**). At the previously used low dose of L-DOPA (1.5 mg/kg, i.p), the male MCI-Park (no virus control) mice showed significantly reduced latency to fall in the accelerating rotarod (82.57 ± 9.25 s, $p<0.0001$) and distance traveled in the open field (5759.19 ± 530.03 cm, $p=0.0100$) compared to their age-matched controls (rotarod: 175.74 ± 11.60 s, open field: 8717.00 ± 256.82 cm; **Figure 5B, left and right panels**). When given the same L-DOPA dose, the male MCI-Park mice that received AiE0450h-AADC-HA showed rescue in the accelerating rotarod (141.27 ± 6.15 s, $p=0.0005$). compared to the no virus control and those injected with AiE0450h-SYFP2 (77.24 ± 8.93 s, $p=0.0002$**; Figure 5B, left panel)**. The AiE0450h-AADC-HA treated MCI-Park mice showed significantly increased total distance traveled in the open field (7166.63 ± 774.61 cm, $p=0.0308$) compared to the MCI-Park mice with AiE0450h-SYFP2 (4671.06 ± 609.93 cm**; Figure 5B, right panel**). RO injection of CMV-AADC-HA resulted in a high mortality rate of the MCI-Park mice, hampering their behavioral assessment due to the lack of sufficient power **(Figure S4B)**.

Similar to the males, the female MCI-Park (no virus control) mice also spent significantly less time on the accelerating rotarod (86.04 ± 4.44 s, $p<0.0001$) as well as showed significantly decreased distance traveled in the open field (4462.48 ± 808.74 cm, $p= 0.0121$) compared to the sex and age-matched controls (rotarod: 195.59 ± 8.33 s, open field: 9130.89 ± 563.27 cm; **Figure 5E, left and right panels**). However, unlike the male counterparts, RO injection of AiE0450h-AADC-HA in the female MCI-Park did not alleviate their motor symptoms at the same low dose of L-DOPA (1.5mg/kg, i.p). Upon increasing the L-DOPA dose to 3 mg/kg, AiE0450h-

AADC-HA significantly improved their performance in the accelerating rotarod (146.56 ± 5.91 s, p<0.0001 for all) compared to no virus control, AiE0450h-SYFP2 (88.96 ± 9.54 s), and AiE0450h-AADC-HA at 1.5 mg/kg dose of L-DOPA (80.70 ± 8.26 s; **Figure 5E, left panel**). Furthermore, at the elevated 3 mg/kg L-DOPA dose, the AiE0450h-AADC-HA treated female MCI-Park mice showed significantly increased total distance traveled in the open field (12428.50 ± 1594.72 cm, p<0.0001 for all) compared to the MCI-park mice with no virus, AiE0450h-SYFP2 (4690.67 ± 764.72 cm), and AiE0450h-AADC-HA at 1.5 mg/kg dose of L-DOPA (5390.75 ± 756.30 cm**; Figure 5E, right panel**). Robust AADC-HA expression was detected in the striatum, VTA/SNc, and LC of both male (**Figure 5C**) and female (**Figure 5F**) MCI-Park mice that received AiE0450h-AADC-HA. As before with the males, RO injection of CMV-AADC-HA increased mortality in the female MCI-Park mice (data combined in **Figure S4B**), strongly supporting the better tolerability and higher effectiveness of the cell-type specific enhancer-driven AADC through systemic route of administration.

Additionally, to compare the viral vectors through direct route of administration, we performed bilateral intra-striatal surgeries in MCI-Park mice at P30-35 and delivered 1e9 vg of the AADC-HA vectors per hemisphere, followed by behavioral testing with low L-DOPA dose (1.5mg/kg, i.p) 4 weeks later (**Figure 5G**)**.** AiE0450h-AADC-HA treated animals showed comparable time spent on accelerating rotarod (155.67 ± 7.14 s, p=0.9096) to the CMV-AADC-HA mice (146.01 ± 15.17 s) and both were significantly better than the no virus control MCI-Park mice (66.52 ± 7.30 s, p<0.0001 for both; **Figure 5H, left panel**). AiE0450h-AADC-HA administration in MCI-Park mice also resulted in significantly greater distance travelled in the open field (9581.95 ± 3111.27 cm, p=0.0383) compared to no virus control MCI-Park mice (3167.62 ± 235.42 cm) while CMV-AADC-HA mice did not show significant increase (7362.13 ± 2024.14 cm, p=0.2206; **Figure 5H, right panel**). AiE0450h-AADC-HA and CMV-AADC-HA showed comparable spread and expression in the dorsal striatum of the mice **(Figure 5I)**. Due to their small size (average body weight <12.5g at p30), the female MCI-Park were excluded from the surgical procedure.

These data demonstrate that AiE0450h-AADC-HA delivery by both invasive and non-invasive routes of administration, in conjunction with L-DOPA, can alleviate major motor deficits in a progressive PD mouse model. CMV-AADC-HA showed rescue of phenotype when delivered directly into the striatum. Furthermore, our data revealed sex-dependent differences in L-DOPA efficacy required to achieve the therapeutic benefit of AiE0450h-enhancer-driven AADC.

Enhancer-targeted AADC expression in other relevant cell types via RO delivery produced selective rescue of PD-associated motor deficits

To determine if viral expression of AADC in other striatal cell types implicated in PD could improve motor outcomes in the presence of L-DOPA, we next developed vectors containing enhancers that selectively target striatal cholinergic interneurons, dopaminergic neurons in the VTA/SNc, and astrocytes. Previously validated enhancers AiE0743m_3xC2, AiE0888m, and AiE0387m_3xC1 were utilized to gain access to striatal cholinergic,[40] dopaminergic (unpublished), and astrocytes,[62] respectively. The same HBB3-containing AADC-HA design was utilized as in the previous constructs (**Figure 6A**). Each construct was packaged into PHP.eB serotyped virus and delivered RO at 1e12 vg into adult wild-type C57Bl6/J mice. After 3 weeks post injection, the mouse brains were collected and sections were co-stained with anti-HA and anti-choline acetyltransferase (anti-Chat) for striatal cholinergic interneurons,[63] anti-TH for midbrain dopaminergic neurons,[49] or anti-glial fibrillary acidic protein (anti-GFAP) for astrocytes[64] (**Figure 6B-D**).

Analyses of the AiE0743m_3xC2-driven AADC-HA revealed transgene expression in striatal cholinergic neurons as expected (white arrows, **Figure 6B, left panel**), as well as expression in the TH+ cells within the VTA (completeness: 37.38 ± 4.26 %, specificity: 43.24 ± 0.54%), SNc (completeness: 72.62 ± 5.26%, specificity: 57.29 ± 5.53 %), and LC (47.94 ± 2.87%, specificity: 63.32 ± 0.97%) as depicted with white arrows (**Figure 6B, middle and right panels and Figure S5A**). The AiE0888m-enhancer drove strong expression of AADC-HA fibers in the striatum (**Figure 6C, left panel**) and in the dopaminergic neurons within the VTA and SNc

(completeness: 61.06 ± 6.36% and 60.33 ± 1.39 % respectively; specificity: 84.35 ± 1.95 % and 83.45 ± 6.17 %, respectively; white arrows, **Figure 6C, middle panel and Figure S5A**). Additionally, it also expressed AADC-HA in TH+ neurons within LC (**Figure 6C, right panel**) with equivalent completeness of 67.17 ± 5.80 % but significantly lower specificity of 62.07 ± 4.41% (p=0.0387 vs VTA and p=0.0458 vs SNc; **Figure S5C**). Finally, we observed strong expression of AiE0387m_3xC1-driven AADC-HA in GFAP+ astrocytes throughout the brain, including in the striatum (white arrows, **Figure 6D, left panel**) and LC (**Figure 6D, right panel**). Interestingly, the AiE0387m_3xC1-driven AADC-HA was also sparsely detected in dopaminergic neurons within the VTA (completeness: 31.29 ± 12.61 %, specificity: 58.20 ± 6.73 %) and SNc (completeness: 53.21 ± 12.26%, specificity: 57.27 ± 15.17 %) (white arrows, **Figure 6D, middle panel and Figure S5A**). Sparse co-labeling of AiE0387m_3xC1-driven AADC-HA was also observed in TH+ neurons in LC (completeness: 20.36 ± 4.43 %, specificity: 31.08 ± 5.03%; white arrows, **Figure 6D, right panel and Figure S5A**). This is consistent with the SYFP2-expressing AAV control at a lower (5e11 vg) dose (https://portal.brain-map.org/genetic-tools/genetic-tools-atlas).

To investigate the efficacy of these viral AADCs for phenotypic rescue in 6-OHDA lesioned animals, we administered the SYFP2 control for each respective enhancer, AiE0743m_3xC2-AADC-HA, AiE0888m-AADC-HA, or AiE0387m_3xC1-AADC-HA viruses at 1e12 vg dose by RO and performed behavioral tests after L-DOPA injection (1.5 mg/kg, i.p.) 3 weeks later (**Figure 6E**). The toxin-lesioned mice that received either AiE0743m_3xC2-AADC-HA (167.11 ± 13.34 s, p<0.0001) or AiE0888m-AADC-HA (149.64 ± 9.23 s, p=0.0029) showed significantly increased latency to fall in accelerating rotarod compared to the SYFP2-controls (105.79 ± 6.97 s), while the AiE0387m_3xC1-AADC-HA did not cause significant increase in their latency (131.54 ± 11.85 s, p=0.2381; **Figure 6F, left panel**). In addition, RO delivery of either AiE0888m-AADC-HA (10210.70 ± 494.52 cm, p=0.0014) or AiE0387m_3xC1-AADC-HA (10154.90 ± 449.68 cm, p=0.0096) resulted in significant improvement in the total distance travelled in open field

compared to the SYFP2-controls (8291.98 ± 273.89 cm), but AiE0743m_3xC2-AADC-HA mice did not show an increase (8702.63 ± 471.64 cm, p=0.8273; **Figure 6F, right panel**).

To assess if these AAV-AADCs might also alleviate the motor deficits in MCI-Park mice, we RO injected AiE0743m_3xC2-AADC-HA and AiE0888m-AADC-HA at the same viral dose to target striatal cholinergic and dopaminergic neurons respectively and performed behavioral tests after L-DOPA injection (1.5 mg/kg, i.p.) 4 weeks later (**Figure 6G**). Unlike the unilateral 6-OHDA model, at the same low L-DOPA dose, AADC expression in the non-MSN cell types of MCI-Park mice did not rescue their motor symptoms. Compared to the age-matched controls (rotarod: 194.63 ± 5.73 s, open field: 9121.13 ± 346.46 cm), the virally treated MCI-Park mice showed significantly lower latency in the accelerating rotarod (AiE0743m_3xC2-AADC-HA: 114.02 ± 8.82 s; AiE0888m-AADC-HA: 110.64 ± 7.12 s; both p<0.0001; **Figure 6H, left panel**) and reduced distance traveled in the open field (AiE0743m_3xC2-AADC-HA: 7420.88 ± 640.15 cm, p=0.0372; AiE0888m-AADC-HA: 5791.73 ± 531.76 cm; p<0.0001; **Figure 6H, right panel**). Together, these data demonstrate that viral expression of AADC in multiple cell-types and circuits can improve motor symptoms in the unilateral toxin model. However, in the MCI-Park mice, only MSN-enhancer-driven expression in the presence of low L-DOPA dose can rescue the major motor deficits. These data suggest that in a progressive disease model striatal MSNs preferentially support AADC-dependent dopamine production at a reduced substrate level. Collective behavioral results are summarized in **Table S1**.

Conserved AiE0450h-driven MSN AADC expression in non-human primates

To assess potential of the AiE0450h-AADC-HA vector for human gene therapy applications, we next evaluated tolerability and specificity in non-human primates (NHP). We performed bilateral intracerebroventricular (ICV) injections of the AiE0450h-AADC-HA or the pan-neuronal and nuclear-enriched hSyn1-SYFP2-H2B (AiP11839) vector[42] at a dose of 1e13 vg/kg. 4-6 weeks post viral injection, the animals were sacrificed, the brains were collected, and sections containing the caudate and putamen were co-stained for AADC-HA and DARPP-32 (**Figure 7A-**

B). ICV administration of AiE0450h-AADC-HA resulted in highly localized AADC-HA within the caudate putamen (**Figure 7A**) while hSyn1-SYFP2-H2B administration at the matched dose and route yielded more widespread nuclear-enriched-SYFP2 expression in both caudate putamen and the cortex (**Figure 7B**). Quantification of AiE0450h-AADC-HA versus hSyn1-SYFP2-H2B viral expression in DARPP-32+ MSNs showed increased specificity (AiE0450h-AADC-HA: 95.23%, hSyn1-SYFP2-H2B: 70.85%) in labeling for the enhancer-based approach (**Figure 7D**). Furthermore, we evaluated the AiE0450h-AADC-HA vector by stereotactic intraparenchymal injection (1e11 vg total) into the macaque caudate and putamen to directly compare to the current clinical route of administration. Direct intraparenchymal injection resulted in a wider area of expression within caudate and putamen but similarly high specificity for DARPP-32+ MSNs (81.06%) as the ICV injection had (**Figure 7C-D**).

Together, these findings demonstrate that the AiE0450h enhancer can restrict AADC-HA expression predominantly to MSNs within NHP caudate and putamen with both intraparenchymal and ICV routes of administration. They also highlight some of the challenges of achieving broad yet specific AADC expression throughout the entirety of the NHP caudate and putamen and demonstrate that the intraparenchymal route achieves much broader transduction, which may be key for many translational applications.

Discussion

We developed a suite of enhancer-based viral tools expressing human AADC and tested them via multiple routes of administration in mouse. These analyses revealed that striatally expressed AADC is also observed in *DDC*-enriched areas outside of the striatum, most notably SNc/VTA and LC, which may reflect trafficking, either at RNA and/or protein levels, or a mechanism yet to be described. Cell type-specific AADC viral expression in combination with low dose L-DOPA rescued select motor phenotypes in two mouse models of PD. Furthermore, the development of LID was greatly attenuated by MSN-enhancer-driven AADC delivery relative to untreated

conditions. Lastly, we showed conserved expression of AADC in MSNs in macaque caudate and putamen following two clinically relevant routes of administration. This data demonstrates the efficacy of enhancer-based viral tools for ameliorating major motor deficits in PD and suggests a potential therapeutic application for the tools to be used in combination with L-DOPA.

Previous studies in which viral AADC was delivered directly into the striatum or caudate/putamen in rodents, non-human primates, or humans, did not evaluate transgene expression brain-wide and had limited cell type characterization even within the injected region.[28,65–67] In the present study, we evaluated transgene expression throughout the brain and found that while AADC-HA was specifically expressed in the enhancer-defined cell types within the striatum, it was also expressed to varying degrees depending on the exact vector and route of administration within the VTA/SNc and LC. While the exact mechanism of this extra-striatal expression is yet to be determined, the strong functional projections between the striatum and midbrain dopaminergic areas may facilitate the transmigration of the therapeutic cargo, at RNA or protein level, either through synaptic transport or gap junctions.[68,69] Similarly, LC has robust connectivity with midbrain dopaminergic areas and ventral striatum[70] and sparser projections to dorsal striatum,[71] which could potentiate viral AADC expression in this area. It is also notable that AADC trafficking appeared most robust following RO injection, suggesting that the viral entry mechanism may promote changes at the cellular level to more greatly facilitate spread. Regardless of the mechanism, unintended AADC expression in residual dopaminergic neurons likely further augments brain dopamine levels and this combined with striatally derived dopamine production, may impart the therapeutic benefit observed in rodent models of PD and in human PD patients. However, in cases of complete dopamine neuron depletion, MSN-limited AADC expression may be sufficient, as we found that intra-striatal administration alleviated the motor deficits in the presence of L-DOPA in the PD mouse models. While the exact mechanism

of DA synthesis in the MSNs has not been fully characterized, transduction of the postsynaptic neurons in the putamen with the AADC enzyme has shown to increase DA production.[23,26,72] Besides providing therapeutic relief from PD-associated motor symptoms, considerable efforts have gone into reducing the side effects of protracted L-DOPA treatment.[8,58,73–75] The short plasma life of L-DOPA,[76] combined with the increasingly longer off-periods of drug efficacy[75,77] as the disease progresses, results in a pulsatile stimulation of dopamine receptors that eventually alters basal ganglia output.[9,11,78,79] To mitigate this issue, the FDA approved an oral formulation of carbidopa/levodopa (CREXONT (IPX203)) in 2024 that combines immediate-release (IR) granules with extended-release (ER) pellets.[80] The same year, a subcutaneous continuous infusion of levodopa prodrugs, delivered via a wearable pump, was also approved for PD therapy (VYALEV).[81,82] While they both reduce on/off times designed to diminish motor fluctuations, there is still room for improvement to get flattened pharmacokinetics and reduce therapeutic dose. Our study showed that MSN enhancer-driven delivery of AADC alleviated LID in toxin-lesioned mice following chronic L-DOPA administration, suggesting that viral expression of AADC in striatal MSNs might help to minimize the fluctuations of the dopamine levels in the brain, thereby reducing the occurrence of LID. Additionally, in the presence of AADC, a lower dose of L-DOPA may be needed to achieve the same therapeutic benefit, which also could delay the onset of dyskinesia, consistent with a clinical study utilizing the ubiquitous promoter.[31] A neuropathological hallmark of PD is the degeneration of nigrostriatal pathways and progressive loss of midbrain dopaminergic neurons.[83] While studies delivering AADC directly to these cells have shown great promise,[61,84] this cell type has largely been excluded from current therapeutic strategies due to the profound degree of loss (~90%) in early-stage PD patients and because of challenges associated with surgically targeting the VTA/SNc in PD patients. New diagnostic assays such as the FDA-approved alpha synuclein seed assay[85] or measures of retinal thickness[86,87] may promote earlier detection where the extent of degeneration is less significant, making targeted intervention of dopaminergic neurons more plausible. Our study

showed that systemic administration of a midbrain dopamine-specific enhancer-AAV not only delivered viral AADC-HA into the remaining TH+ neurons in VTA/SNc of the toxin-lesioned mice and showed strong expression of AADC-HA in the striatal projections but also rescued the motor deficits of the unilateral PD mouse model. Consistent with the previous studies, [61,84] these data demonstrate that surviving dopaminergic neurons might be sufficient to improve motor symptoms in PD.

The large, spiny cholinergic interneurons, comprising only about 1% of striatal population, are considered master regulators due to their widespread connectivity throughout the striatum[88] and have been identified as affected cell type in PD.[89,90] Systemically delivering viral AADC to these neurons in unilateral lesioned animals alleviated major motor phenotypes in the presence of low dose of L-DOPA. However, the impact of AADC expression in striatal cholinergic cells alone needs to be investigated further due to the observed migration of the therapeutic cargo to the midbrain and LC. Additionally, astrocytes play critical roles in L-DOPA uptake and metabolism,[91,92] which makes them promising candidates for targeted PD therapy. So, in addition to non-DA neurons, we showed that systemic delivery of AADC to astrocytes throughout the brain in combination with L-DOPA could also successfully relieve the motor symptoms. Collectively, this data suggests that multiple cell type environments may promote AADC-mediated elevations in brain dopamine levels and in turn symptomatic improvement, thereby expanding the possibilities for cell type-specific therapeutic interventions. It is notable however that in the model that most closely recapitulates the human PD condition, the MCI-Park model, only MSN-enhancer-driven AADC-AAV was effective at phenotypic rescue. While differences exist between the PD models such as unilateral vs bilateral depletion and potential inflammatory states, these data suggest that targeting AADC to MSNs may be essential for functional restoration in the face of progressive neurodegeneration.

Our study further highlighted certain sex-dependent differences in the progressive, genetic mouse model where the diseased female mice required higher doses of L-DOPA to achieve the

same benefit of the viral AADC as the male mice. These data appear consistent with findings in humans suggesting that male patients have a higher prevalence of PD whereas female patients experience faster disease progression, longer L-DOPA wearing-off periods, and greater risk of dyskinesia.[93–95] Various molecular and physiological variables like estrogen levels, L-DOPA clearance rate, urate levels[95–97] have been shown to underlie such sex-based differences and may contribute to the observations in the present study. These differences underscore the necessity of sex-balanced studies, as well as careful dosing studies, to enable more tailored therapeutic interventions.

In summary, this study constitutes the first successful application of cell-type specific enhancer-driven AADC for the treatment of PD, demonstrating robust rescue of motor phenotypes associated with the disease and reduction of the side-effects due to prolonged usage of L-DOPA. These versatile, cell type-selective agents can be paired with leading BBB-penetrant capsids for less invasive delivery or administered to the brain for precise targeting. This potential strategy lays out the groundwork for the next generation of targeted therapeutics for PD.

Resource availability

Lead Contact

Further information and requests for resources and reagents should be directed to and will be fulfilled by the Lead Contact, Tanya L. Daigle (tanyad@alleninstitute.org).

Materials availability

All plasmids generated in this study are in process to be deposited to Addgene.

Key Resource Table (refer to Table S2)

Experimental model and subject details

Mouse breeding and husbandry

For vector validations and the 6-OHDA toxin experiments, adult C57Bl/6J mice were bred and housed under Institutional Care and Use Committee (IACUC) protocols 2202 and 2505 at the Allen Institute, with no more than five animals per cage, maintained on a 12 day/night cycle, with food and water provided *ad libitum*. Enrichment, such as plastic shelter and nesting materials, were provided. Adult C57BL/6J mice were also purchased directly from The Jackson Laboratory (Strain #000664, RRID: IMSR_JAX:000664) as needed and housed at the Allen Institute under the same conditions. Both male and female mice were used for experiments, and the minimal number of animals was used for each experimental group. Animals with anophthalmia or microphthalmia or other obvious conditions (e.g. penile prolapse) were excluded from experiments.

Mice carrying homozygous floxed *Ndufs2* (*Ndufs2*$^{fl/fl}$) were crossed with double heterozygous mice expressing Cre recombinase (Cre) under the control of the DA transporter (DAT, encoded by *Slc6a3*) promoter (*Slc6a3*$^{+/cre}$) as well as one floxed allele of *Ndufs2 (Ndufs*2$^{+/fl}$) on a C57BL/6J background. This breeding scheme allowed us to generate both MCI-Park mice (*Slc6a3*$^{+/cre}$; *Ndufs2*$^{fl/fl}$) and age-matched littermate controls expressing floxed *Ndufs2* in the absence of Cre recombinase (*Slc6a3*$^{+/+}$; *Ndufs2*$^{fl/fl}$) while deriving future double heterozygous breeders. To create our in-house parent lines, heterozygous *Slc6a3-cre* mice (B6.SJL-*Slc6a3*$^{tm1.1(cre)Bkmn}$/J; Strain#:006660, RRID:IMSR_JAX:006660) and homozygous floxed *Ndufs2 mice (Ndufs2*$^{tm1.1Job}$ *Slc6a3*$^{tm1.1(wt)Bkmn}$*/SurmJ;* Strain#:036313, RRID:IMSR_JAX:036313) were obtained from the Jackson Laboratories, bred and housed under IACUC protocols 2202 and 2505 at the Allen Institute.

Macaque husbandry

Surgical procedures, experimental protocols and animal care conformed to the NIH Guide for the Care and Use of Laboratory Animals and were approved by the Institutional Animal Care and Use Committee at the University of Washington. IACUC Protocol Number 4532-10. Animal husbandry and housing were overseen by the Washington National Primate Research Center.

Monkeys had *ad libitum* access to biscuits (Lab Diet, Fiber Plus Monkey Diet Cat#5049) and controlled daily access to fresh produce, treats and water. When possible, animals were pair-housed and allowed grooming contact. Cages were washed every other week, bedding was changed every day, and animals were examined by a veterinarian at least twice per year and as needed.

Methods details

Viral vector construction

All recombinant AAV vectors (rAAV) backbones contained inverted terminal repeats (ITRs) required for viral packaging, a woodchuck hepatitis virus posttranscriptional regulatory element (WPRE3) to enhance expression, and the bGH polyadenylation signal for transcript stability. The previously reported rAAV-AiE0450h-minBG-SYFP-WPRE2-bGHpolyA (AiP12236) served as the initial template.[40]

For vectors encoding *DDC* (AiP13663, AiP16328, AiP13912, AiP13742, AiP15007, AiP16392, AiP16391, AiP16390), the open reading frame was optimized using the Integrated DNA Technologies (IDT) Codon Optimization Tool followed by additional rounds of manual editing to facilitate gBlock synthesis and improve stability. These refinements included reducing GC-rich domains, eliminating long or repetitive elements, and removing predicted cryptic splice donor/acceptor motifs, TATA-like sequences, homopolymeric WWWWWW tracts, and CpG-rich regions.

For constructs that contained an intron (AiP13663, AiP16328, AiP13742, AiP15007, AiP16392, AiP16391), the intron was inserted at the first high-confidence splice donor/acceptor site (CAG^G) within the open reading frame to promote higher expression.

All plasmids were generated using standard molecular cloning techniques and were amplified in One Shot™ Stbl3™ chemically competent *E. coli* (Thermo Fisher Scientific, Cat. #C737303) at

32 °C, purified using the HiSpeed Plasmid Maxi Kit (Qiagen, Cat. #12663) and validated by full plasmid sequencing with Plasmidsaurus® (Oxford Nanopore platform).

Viral packaging and titering

Iodixanol-gradient purified rAAVs of the PHP.eB serotypes (AiE0450h-AADC(no intron)-HA; AiP16390, AiE0450h-AADC(SV40 small-t)-HA; AiP16391, AiE0450h-AADC(SV40)-HA; AiP16392) were generated in house using previously described methods.[39,43] The average titer of these viral preps was 5.0 X 10^{13} vg/mL (ranging from 3.92-7.78 X 10^{13} vg/mL) and were quantified using droplet digital PCR (QX 200, Bio-Rad) by targeting the ITR sequences. The following primers and probes were used: forward primer 5′-GGAACCCCTAGTGATGGAGTT-3′, reverse primer 5′-CGGCCTCAGTGAGCGA-3′, and probe 5′-/56-FAM/CGCGCAGAG/ZEN/AGGGAGTGG/3IABkFQ/-3′.

AiE0450h-SYFP2; AiP12236, AiE0450h-AADC-HA; AiP13663, CMV-AADC-HA; AiP16328, AiE0743m_3xC2-AADC-HA; AiP13912, AiE0888m-AADC-HA; AiP13742, and AiE0387m_3xC1-AADC-HA; AiP15007 purified viruses were packaged by PackGene Biotech at the titer of 2.0 x 10^{13} vg/mL, quantified using qPCR with the same primer set as above.

Mouse retro-orbital (RO) injections of AAVs

Mice were briefly anesthetized with isoflurane and 1e10^{12} vg were delivered into the right venous sinus in a volume of 90µL via RO injection. 0.5% proparacaine hydrochloride ophthalmic solution (Bausch+Lomb, Cat# 24208-730-06) was then applied to the injected eye. Tissue samples were collected for analysis 3-4 weeks post-injection.

Mouse stereotactic surgeries

6-OHDA toxin surgeries:

Pre-operative care started a week prior to surgery, where supplementary food was provided in a limited amount to both vehicle-control and toxin-lesion mice (P70) to increase their body weights to ≥ 28 g on surgery date. Supplementary foods consisted of DietGel Boost (Clear H_2O, 370

Kcal/g) and D12492i Rodent Diet (Research Diets, 60 % kcal fat). This supplementary food was discontinued upon recovery by 10-14 days (weight stabilization post-surgery).

Mice were anesthetized with 4 % isoflurane and maintained at 1.5-2 % in a stereotaxic frame (Kopf 1900) equipped with a heating pad (37 °C) to maintain their body temperature. At the start of the surgery, all mice were injected subcutaneously with 500 µL of LRS (Lactated Ringers Solution, Vedco) and 5 mg/kg carprofen (Rimadyl, Zoetis, Cat# 151-199). Ophthalmic ointment (Systane, Alcon) was applied to the eyes to prevent corneal drying. The lesion was induced in right dorsal striatum by injecting 1.5 µL of 6-OHDA hydrochloride (H4381, Sigma Aldrich) at a concentration of 3 µg/µL dissolved in sterile 1x PBS with 0.2 % ascorbic acid (A7506, Sigma Aldrich), according to the following coordinates (mm from bregma): anteroposterior (AP) +0.26; mediolateral (ML) +2.00; and dorsoventral (DV) −3.4 (from skull). Control mice received a sham lesion, consisting of unilateral injections of 1.5 µL of vehicle (0.2 % ascorbic acid in sterile 1x PBS). The rate of infusion was maintained at 150 nL/min with a Nanoject II Nanoliter Injector (Drummond, Cat#3-000-204) and Micro4 Controller (World Precision Instruments, SYS-MICRO4), and after infusion, the glass capillary was kept at the injection site for 5 minutes before being withdrawn slowly to avoid efflux. Post injection, the mice were returned to the home cage kept on a heating pad (37 °C) to recover for an hour before returning them to vivarium.

Intra-striatal viral surgeries:

The injections were performed bilaterally in the dorsal striatum, according to the following coordinates (mm from bregma): anteroposterior (AP) +0.26; mediolateral (ML) +/- 2.00 and dorsoventral (DV) −3.4 (from skull). Viral vectors were thawed and diluted 1:10 with sterile 1x PBS solution to reach 2e12 vg. 500 nL (final 1e9 vg) was delivered to both the hemispheres at the rate of 100 nL/min while undiluted vector (2e13 vg) was injected for the high dose (final 1e10 vg) experiment. The remainder of the procedure was performed the same as before.

Mouse behavioral phenotyping

Acclimation: Adult mice (P60-100, depending on the PD model) were used for behavioral testing. All tests were conducted in the light phase. Mice were placed in the testing room with reduced light density to acclimate for at least 30 minutes in home cages before each paradigm. All tests were run on different days and counterbalanced to avoid the inter-behavioral effect as well as possible L-DOPA interaction. The testing equipment was cleaned with Peroxigard (Virox Technologies Inc.) and/or 70% ethanol and air dried between mice.

L-DOPA preparation:

Levodopa (Sigma Aldrich, PHR1271) was used to prepare the L-DOPA solution (in 0.9% sterile saline) at the doses mentioned in the paper (1.5 mg/kg to 20 mg/kg, depending on the experiment). A peripheral decarboxylase inhibitor, Benserazide (12 mg/kg, B7283, Sigma Aldrich), was always added to the preparation to inhibit the enzyme DOPA decarboxylase in the body's periphery, increasing the L-DOPA content in the brain.[98] L-DOPA/Benserazide drug solution should be made fresh daily before injections, if possible, or stored in light-protected condition at 4 °C up to 48 hours. The mice were always placed in behavioral apparatus 45 mins post- L-DOPA/Benserazide intraperitoneal administration, either after a single injection or on the last day of the prolonged application.

Accelerating Rotarod:

Rotarod accelerating from 4–40 rotations per min over 300 s was used (ENV-574M, Med Associates) to test their motor behavior. Mice were run for three trials with 3 min inter-trial interval. Each trial ended if mice fell off the rod, started rotating with the rod for one whole rotation, or successfully stayed on rod for the full 300 s. The rods, walls, and fall containers were cleaned with 70% ethanol and air dried before and after each trial. The behavioral performance (latency to fall) was quantified as the average of the three trials.

Open Field:

General locomotor behavior of freely moving mice was evaluated in multi-unit open field boxes (EthoVision XT, Noldus), each box measuring 40 x 40 x 30 cm. The mice were video recorded for 30 minutes during which the body center point of each mouse was live tracked and total distance traveled was compared using EthoVision XT (Noldus, RRID:SCR_000441) software.

Cylinder test:

A clear acrylic (McMaster-Carr) cylinder of 20 cm (diameter) and 30 cm (height) was used to evaluate the frequency of paw touches during explorative activity, to observe and quantify asymmetric behaviors like rotations, dragging of feet, and falling on one side, and to score abnormal involuntary movements in LID. The test apparatus was placed in front of a mirror to observe the mice from all angles. Every session was video recorded for 10 minutes to be analyzed by an experimenter blind to the groups. The room was dimly lit during the entire trial and the walls and floor of the cylinder were cleaned with Peroxigard (Virox Technologies Inc.) and air dried between mice.

Contralateral paw touches:

Forelimb use during supported rearing was assessed by scoring the number of load-bearing contacts on the cylinder wall. Individual contact was counted when the mouse returned to a resting position and reared again to touch the cylinder wall. Only the initial contact was marked as ipsilateral first or contralateral first or both simultaneously, regardless of whether they used or took off the second paw afterwards. Ipsilateral and contralateral were defined relative to the 6-OHDA-lesioned side. Percent contralateral paw touches were calculated as [contralateral first) /total observations] * 100.

Contralateral rotations:

Videos recorded in the cylinder were further analyzed to quantify the total number of ipsilateral and contralateral turns to the lesion over 10 minutes. 180-degree turns were scored as one,

while 360-degree turns were scored as two.[99,100] Net contralateral turns were calculated as [total contralateral - total ipsilateral].

Abnormal involuntary movements (AIMs):

Videos recorded in the cylinder were used to assess abnormal involuntary movements (AIMs) as defined in previous studies.[8,56,99] Each mouse was observed individually for the entire duration of 10 mins by an experimenter blinded to the groups. The AIMs were classified into three different categories based on their topographic distribution: (i) axial AIMs- twisting of the neck and upper body towards the side contralateral to the lesion. Unlike the rotations described earlier, these were characterized by the absence of full body turns. (ii) orolingual AIMs- empty jaw movements, lip smacking, and tongue protrusion; (iii) forelimb AIMs- brisk, purposeless movements of the contralateral forelimb, sometimes combined with empty grabbing movement or tapping of the paw. Instead of separating the categories into subtypes based on AIM severity scale,[56] the occurrences were evaluated as presence and absence of the dyskinetic phenotype. Each individual incidence was counted from start of an event to end of the event when the mouse returned to a resting position and classified into the three categories defined earlier. Though rare, if within one incidence, more than one category of AIMs occurred, each would be counted separately. The hyperkinetic and dystonic movements had to be involuntary, insistent, and clearly distinguished from naturally occurring behaviors like grooming, sniffing, rearing and gnawing for them to be considered in quantification. The classifications and values were randomly checked by another blinded experimenter. Total occurrence of AIMs was calculated by adding the number of incidences in the three defined types over 10 mins.

Immunostaining

Mice were transcardially perfused with 4 % PFA (paraformaldehyde) in 1x PBS. After perfusion, tissues were kept in the fixation solution overnight at 4 °C, then transferred to 30 % sucrose solution for 24 hours. Using a freezing microtome (Leica SM2000R, RRID:SCR_018456), tissue

was mounted on OCT medium (Tissue-Tek® O.C.T. Compound Cat# 4583), sectioned (50 µm thickness) and collected free-floating.

Sections were washed three times in 1x PBS at room temperature and were blocked in 1x PBS containing 5 % normal goat serum (Vector Laboratories, Cat# S-1000-20), 0.2 % Triton X-100 (Millipore Sigma, Cat# X100), 2 % bovine serum albumin (Millipore Sigma, Cat# A9418-5G) for 1 hour at room temperature. Sections were then incubated overnight at 4 °C in the same blocking solution containing primary antibodies: Chicken Anti-Tyrosine Hydroxylase antibody (1:500; AB76442, Abcam, RRID:AB_10412418), HA-Tag (C29F4) Rabbit mAb (1:1000; 3724, Cell Signaling Technology, RRID:AB_1549585), Purified Mouse Anti-DARPP-32 (1:500; 611520, BD Biosciences, RRID:AB_398980), Anti-CHAT Antibody Mouse IgG2B Clone CL3173 (1:500; AMAb91130, Atlas Antibodies, RRID:AB_2665812), Anti-Glial Fibrillary Acidic Protein Antibody, clone GA5 in Mouse (1:1000; MAB360, Millipore Sigma, RRID:AB_3695585). After primary incubation, sections were washed three times in 1x PBS and incubated in the same blocking solution containing DAPI (1:1000; Fisher Scientific, Cat# 62248) and secondary antibodies: Goat α- Rabbit IgG AF488 (1:1000; A11008, Thermo Fisher Scientific, RRID:AB_143165), Goat α-Mouse IgG12B AF555 (1:500; A21147, Thermo Fisher Scientific, RRID:AB_2535783), Goat α-Chicken IgY AF568 (1:500; A11041, Thermo Fisher Scientific, RRID:AB_2534098), Goat α-Rabbit IgG AF568 (1:1000; A11011, Thermo Fisher Scientific, RRID:AB_2534078), Goat α-Mouse IgG1 AF647 (1:500; A21240, Thermo Fisher Scientific, RRID:AB_2535809) for 2 hours at room temperature. Following secondary incubation, sections were washed three times in 1x PBS. All steps were performed under gentle agitation. Stained tissue was mounted onto Superfrost slides (Fisher Scientific, Cat# 12-550-15) with ProLong Gold antifade reagent (Invitrogen, Cat# P36930, RRID:SCR_015961).

Imaging

Images were acquired with a Nikon Eclipse Ti2 epifluorescence microscope and a Zeiss LSM 880 confocal microscope using manufacturer's software. Whole section images were acquired

with a 10x objective using the same intensity and exposure time across samples at a resolution of 512x512. Z-stacks were collected in 6μm increments and collapsed into maximum intensity projections using manufacturer's software. Higher magnification images were acquired with a 20x objective using the same intensity and exposure time across samples at a resolution of 1024x1024. Z-stacks were collected in 1 μm increments and collapsed into maximum intensity projections using Imaris software (Bitplane 10.0.1, RRID:SCR_007370). Brightness, contrast, and pseudo-coloring were matched across images using Imaris tools. For quantification, the brightness and contrast were kept uniform across all images and spots were identified for individual channels using the automated Imaris spot detection (10 μm) with background subtraction applied. Colocalization was assigned automatically with a constant shortest distance to spots (<10 μm). Percent completeness of AADC-HA labeling was calculated by taking the number of double-positive cells (i.e., HA+ and TH+) and dividing that by the total number of TH+ cells. Percent specificity was calculated by taking the number of double-positive cells (i.e., HA+ and TH+) and dividing that number by the total number of virally labeled cells (i.e., HA+).

Intraparenchymal and intracerebroventricular injections of AAV vectors into macaque, histology, immunochemistry, and imaging

All procedures used with macaque monkeys conformed to the guidelines provided by the US National Institutes of Health and were approved by the University of Washington Animal Care and Use Committee. Three male southern pig-tailed macaques (Macaca nemestrina), between the ages of 2-3 years, weighing ~3 kg were used in this study for intracerebroventricular (ICV) and intraparenchymal (IP) injection of iodixanol gradient purified enhancer-AAV vectors were packaged by PackGene Biotech.

Vectors for IP injections were delivered using the Brainsight robotic surgery system (Rogue Research) for precision targeting. Brain MRIs for each animal were acquired and utilized for pre-planning of virus injection surgery using the Brainsight vet robot software v2.5 (Rogue Research). On the day of surgery, the animals were deeply anesthetized and positioned with

their heads in the stereotaxic frame of the Brainsight surgery platform. A skin incision was made to expose the top of the skull, and burr hole craniotomies were drilled over the planned injection trajectory locations under the guidance of the Brainsight robotic surgery arm. After craniotomy, a prefabricated steel cannula with PE tubing attachment was loaded with a total of 20 μL of AAV vector and attached to the robotic arm. A total of 5 μL of virus was injected into left putamen and left caudate. 1 μL of virus was gradually injected at five depths with 1mm spacing as the cannula tip was retracted dorsally. At the end of the final injection point in each track, the cannula was left in place for 10 min to allow virus diffusion prior to extracting the cannula from the brain. Note that additional virus injection sites were made in other distal brain locations in each macaque, but striatal labeling remained physically clearly separated from distal injection sites.

For bilateral ICV injections, brain MRIs for each animal were acquired and utilized for pre-planning of virus targeting and delivery based on coordinates. On the day of surgery, the animals were deeply anesthetized and positioned with their heads in the stereotaxic frame. A skin incision was made to expose the top of the skull, and a burr hole craniotomy was drilled a few millimeters off the midline at the predetermined coordinates, bilaterally. A 22-gauge spinal needle was mounted on the stereotactic arm and positioned over the craniotomy Dura was nicked and the needle was lowered through the burr hole to preplanned injection coordinates. Lateral ventricle access was verified by drawing CSF into the syringe. Upon confirmation of correct needle placement, 1e13 vg/kg virus solution was loaded into the syringe and 1.55 to 1.75 mL of solution was manually infused over the period of 1 hour. Upon completion, the needle was removed, and the brain surface was rinsed with a sterile saline solution. A piece of DuraGen (Integra, USA) was fitted into the burr hole to cover the opening. The subcutaneous tissues and skin were sutured closed, tissue adhesive (3M Vetbond Tissue Adhesive, Cat#1469) was applied, and incisional bupivacaine was administered. After the surgery, animals were placed in individual cages overnight for post-op monitoring and introduced back into their social

groups after recovery by the staff of the Washington National Primate Research Center (WaNPRC).

Around 30 days post-injection, all animals were sacrificed via transcardial perfusion with 2 L NMDG-aCSF solution per subject. The brain was then removed and rapidly transported from the WaNPRC to the Allen Institute in chilled NMDG-aCSF solution for further tissue processing. The brain was first hemisected and drop-fixed in freshly prepared 4 % PFA in PBS for 48-72 hours at 4 °C. After PFA fixation, the brain was transferred into 1x PBS +0.01 % sodium azide solution. The brain hemispheres were examined and then 0.5 cm thick coronal slabs were cut through the striatum regions. Serial brain slabs were trimmed to fit into the wells of a six well tissue culture plate and submerged in 30 % sucrose solution for a minimum of 48 hour before further processing for histological analysis. Tissue slabs were mounted on the stage of a freezing-sliding microtome (Leica model SM2010R) on OCT medium (Tissue-Tek® O.C.T. Compound Cat# 4583), and sub-sectioned to 30 µm thickness and stored in 1x PBS +0.01 % sodium azide solution. Sections in the region of interest were selected for free-floating immunostaining using the following antibodies: chicken anti-GFP IgY (1:2000; Aves, Cat# GFP-1020, RRID: AB_10000240), mouse anti-DARPP-32 IgG1 (1:500; BD Biosciences, Cat# 611520, RRID: AB_398980), and rabbit anti-NeuN (1:1000; Millipore, Cat#ABN78, RRID:AB_10807945). Secondary antibodies were as follows: Alexa 488 conjugated goat anti-chicken IgY (1:1000; A11039, Thermo Fisher Scientific, RRID:AB_2534096), Alexa 647 conjugated goat anti-mouse IgG1 (1:1000; A21240, Thermo Fisher Scientific, RRID:AB_2535809) and DAPI (1:1000; Fisher Scientific, Cat# 62248). Sections were dried onto 2x3” slides Brain Research Laboratories slides (Cat#5075-W) on a slide warmer and cover-slipped with Prolong Gold Antifade reagent (Invitrogen, Cat# P36930). Images were acquired on a Zeiss LSM 880 confocal microscope or a Nikon Eclipse Ti2 epifluorescence microscope using the manufacturer’s software. Image post-processing, including pseudo-coloring, thresholding, and global brightness and contrast adjustments, was performed uniformly across the entire image using ImageJ (NIH, RRID:

SCR_003070). Percent specificity of AADC-HA labeling was calculated by taking the number of double-positive cells (i.e., HA+ and DARPP32+) and dividing that number by the total number of virally labeled cells (i.e., HA+).

Western Blot

Mice were euthanized without anesthetics by cervical dislocation followed by rapid decapitation. Dissected brain regions were flash-frozen in liquid nitrogen and stored at -80°C until processing. Samples were sonicated in 200 uL of 95 °C 1% SDS with protease inhibitors (Thermo Fisher Scientific, Cat#78441), using previously described methods.[101] Protein levels were assessed using a BCA kit (Thermo Fisher Scientific, Cat#23225) and lysate was denatured by combining with 4x Laemmeli buffer containing 5% BME and then boiled at 95 °C for 5 mins. 50 ug of protein was loaded into 10% Tris/Glycine gels (Thermo Fisher Scientific, Cat#XP00100BOX) and then transferred onto nitrocellulose membranes (Thermo Fisher Scientific, Cat#88025) for 2.5 hours at 25V and at 4 °C. Membranes were blocked in TBS with 5 % BSA for 1 hour at room temperature, then incubated overnight at 4 °C with primary antibodies in TBS containing 0.05 % Tween-20 and 5 % BSA. Primary antibodies included anti-HA (1:500; Biolegend, Cat#901513 , RRID:AB_2565335), anti-AADC (1:500; Cell Signaling Cat#13561S, RRID:AB_2798255), anti-actin (1:1000; Millipore, Cat#MAB1501R, RRID: AB_2223041), and anti-DARPP-32 (1:500; BD Biosciences, Cat#611520, RRID:AB_398980). After washing in TBS with 0.1 % Tween-20, membranes were incubated with fluorescent secondary antibodies (1:10,000 each; Ms 680 and Rb 800; LI-COR, Cat#926-68072, RRID:AB_10953628 and 926-32213, RRID:AB_621848) in LI-COR TBS blocking buffer (Cat#927-60001), washed, and imaged using an Odyssey Infrared Imaging System (LI-COR). Protein signals were quantified using LI-COR analysis software and normalized to actin.

Statistical Analyses

Statistical analyses were conducted using GraphPad Prism 10.4.1 (Dotmatics/GraphPad Software, RRID:SCR_002798) and graphical illustrations were created using BioRender (RRID:SCR_018361). When the data is represented as box plots, the boxes indicate 25th to 75th percentiles and median as the solid line with whiskers denoting minimum and maximum values. When the data is represented as bar graphs, the error bars indicate the standard error of the mean (SEM). Sample size (*n*) refers to biological replicates unless specified in legends. Statistical significance was assessed by unpaired- t test (two-tailed), Mann-Whitney, one-way ANOVA, and two-way ANOVA, where appropriate, followed by the post-hoc tests indicated in the legends. Normality was tested by Shapiro-Wilk and Kolmogorov-Smirnov tests. The level of significance was set at $p<0.05$. Data points deviating more than 2 SD values from the mean were excluded from the analyses.

Data availability Statement: Data associated with this study are present in the paper or the Supplemental Materials. Further data is available from the corresponding author upon reasonable request.

Acknowledgements

We thank members of the Allen Institute animal care team and the Washington National Primate Research Center for providing animal care, surgical support, and assistance with tissue collection for the study. We thank Dr. Rui Costa for kindly sharing the MCI-Park transgenic lines and Dr. D. James Surmeier for critical comments on the manuscript. Many schematics were created with BioRender.com. Research reported in the publication was solely supported by the Paul G. Allen Foundation. We thank the Allen Institute founder, Paul G. Allen, for his vision, encouragement, and support.

Author contributions

T.L.D, J.T.T. and A.C. designed the study. J.K.M., X.O-A., R.M., and A.C.H. designed and constructed vectors. A.C., A.F., and N.T. performed mouse histology and analyses. M.A.Q. performed biochemistry and analyses. A.C., A.F., M.D., and E.K., performed mouse injections, behavior, and analyses. N.T., V.O., M.N.L., G.D.H. and J.T.T., performed macaque injections and histology and analyses. M.R., E.L., L.S., D.R., C.H., B.C., M.L., O.H., T.H., T.W., N.U., C.B., and J.B. performed perfusions, dissections, and provided mouse health support. D.N., R.K., S.K., N.D., and S.Y. performed in-house viral production. K.R., and V.W. performed genetic model breeding, colony maintenance, genotyping, and provided mouse health support. K.G. provided program management support. T.L.D, J.T.T., E.S.L., and B.P.L. provided leadership. A.C., T.L.D., and M.A.Q. wrote the manuscript with support from many co-authors.

Declaration of interests

T.L.D., A.C., E.S.L, J.T.T., B.P.L., and J.K.M. are inventors on one or more U.S. provisional patent applications related to this work. B.P.L., E.S.L., and J.K.M. are founders of Epicure Therapeutics. All authors declare no other competing interests.

Main Figures and Legends

Figure 1: Development and validation of cell-type selective AADC expressing AAVs

(A) Schematic showing the vector designs for AiE0450h-SYFP2, AiE0450h-AADC-HA, and CMV-AADC-HA.

(B) Schematic for retro-orbital (RO) injection and representative sagittal images of SYFP2 (green) and TH (red) for the enhancer control vector (AiE0450h-SYFP2; AiP12236, left panel); AADC-HA (green) and TH (red) for the cell type-specific vector (AiE0450h-AADC-HA; AiP13663, middle panel) and the ubiquitous promoter-driven vector (CMV-AADC-HA; AiP16328, right panel), following RO administration. Top panels: low magnification (10X) stitched, scale bars, 500 μm; bottom panels: low magnification (10X) zoomed into the striatum, VTA/SNc, and LC in

that order, scale bars, 50 μm. Box depicts ROI. TH co-staining was used to designate the relevant areas.

(C) *Ddc* ISH data from the Allen Brain Atlas to visualize Ddc expression in VTA/SNc and LC.

(D) Representative striatal (AP = +0.14 to +0.26 from bregma) coronal images of SYFP2 (green) and DARPP-32+ MSNs (magenta) for AiE0450h-SYFP2 (left panel); AADC-HA (green) and DARPP-32+ MSNs (magenta) for AiE0450h-AADC-HA (middle panel) and CMV-AADC-HA (right panel), following 1e12 vg RO administration. (E) Representative midbrain (AP = -2.92 to -3.08 from bregma) and (F) LC (AP = -5.40 to -5.52 from bregma) coronal images of SYFP2 (green) and TH+ cells (red) for AiE0450h-SYFP2 (left panel); AADC-HA (green) and TH+ cells (red) for AiE0450h-AADC-HA (middle panel) and CMV-AADC-HA (right panel). Low magnification (10X) stitched, scale bars, 500 μm; High magnification (20X), scale bars, 10 μm for the striatum and 20 μm for VTA and LC. White arrows depict representative colocalized cells.

(G) Representative western blot of striatal tissue punches from non-injected and injected mice showing HA and actin bands (top panel), AADC bands (middle panel), and merged image (bottom panel) with HA (green) and viral AADC (vAADC; red) overlaying. The endogenous AADC (eAADC) appears as a lower-molecular-weight band. Actin was used as a loading control.

(H) Quantification of HA expression normalized to AiE0450h-AADC-HA. Data represented as box plots indicating 25th to 75th percentiles and median as the solid line with whiskers denoting minimum and maximum values. n = 4 per condition. The *p* value were calculated by Welch's t-test. $***p < 0.001$

(I) Quantification of vAADC expression normalized to eAADC. Data represented as box plots indicating 25th to 75th percentiles and median as the solid line with whiskers denoting minimum and maximum values. n = 4 per condition. The *p* value was calculated by Welch's t-test. $***p < 0.001$

Figure 2: Retro-orbital administration of AiE0450h-AADC-HA rescued specific motor behaviors in 6-OHDA unilateral toxin model

(A) Schematic overview of the injections and the behavioral tests. 6-OHDA toxin was stereotactically injected into the right dorsal striatum of P70 mice. Three weeks after the surgery, they received a retro-orbital injection of the viral vectors, and a series of behavioral tests were performed three weeks later, 45 mins after either saline or L-DOPA intraperitoneal injection as noted.

(B) Retention time of the mice in the accelerating rotarod test (left), quantification of total distance traveled in the open field test (middle), and quantification of the first load-bearing use of contralateral paw (as percentage out of total paw touches) during rearing in a cylinder (right) in the absence of L-DOPA. Data represented as box plots indicating 25th to 75th percentiles and median as the solid line with whiskers denoting minimum and maximum values. n = 8 per group. The *p* values were calculated by one-way ANOVA followed by Dunnett's post hoc test. $*p < 0.05$, $**p < 0.01$, $***p < 0.001$.

(C) Retention time of the mice in the accelerating rotarod test (left), quantification of total distance traveled in the open field test (middle), and quantification of the first load-bearing use of contralateral paw (as percentage out of total paw touches) during rearing in a cylinder (right) in the presence of L-DOPA. Data represented as box plots indicating 25th to 75th percentiles and median as the solid line with whiskers denoting minimum and maximum values. n = 10-18 for rotarod and open field, n = 8-14 for paw touches. The *p* values were calculated by one-way ANOVA followed by Tukey's post hoc test. $*p < 0.05$, $**p < 0.01$, $***p < 0.001$, $****p < 0.0001$.

Figure 3: Intra-striatal administration of AiE0450h-AADC-HA and CMV-AADC-HA rescued specific motor behaviors in 6-OHDA unilateral toxin model

(A) Representative striatal (AP = +0.14 to +0.26 from bregma) coronal images of AADC-HA (green) and DARPP-32+ MSNs (magenta) for AiE0450h-AADC-HA (right panel) and CMV-AADC-HA (left panel), following 1e9 vg intra-striatal administration. (B) Representative midbrain

(AP = -2.92 to -3.08 from bregma) and (C) LC (AP = -5.40 to -5.52 from bregma) coronal images of AADC-HA (green) and TH+ cells (red) for AiE0450h-AADC-HA (right panel) and CMV-AADC-HA (left panel). Low magnification (10X) stitched, scale bars, 500 μm; High magnification (20X), scale bars, 10 μm for the striatum and 20 μm for VTA and LC. White arrows depict representative colocalized cells.

(D) Representative western blot from striatal tissue punches showing expression of transgene produced HA tag and the loading control actin (top panel), viral AADC (vAADC) and endogenous AADC (eAADC) (middle panel). Bottom panel shows HA and vAADC overlap.

(E) Quantification of fold-change in HA expression normalized to AiE0450h-AADC-HA. Data represented as box plots indicating 25th to 75th percentiles and median as the solid line with whiskers denoting minimum and maximum values. n = 5 per condition. The *p* value was calculated by Mann-Whitney test. $*p < 0.05$

(F) Quantification of vAADC expression normalized to eAADC. Data represented as box plots indicating 25th to 75th percentiles and median as the solid line with whiskers denoting minimum and maximum values. n = 5 per condition. The *p* value was calculated by Welch's t-test.

(G) Schematic overview of the injections and the behavioral tests. 6-OHDA toxin was stereotactically injected into the right dorsal striatum of P70 mice. Three weeks after the surgery, the viral vectors were administered bilaterally to the dorsal striatum, and a series of behavioral tests were performed three weeks later, 45 mins after L-DOPA intraperitoneal injection.

(H) Retention time of the mice in the accelerating rotarod test (left), quantification of total distance traveled in the open field test (middle), and quantification of the first load-bearing use of contralateral paw (as percentage out of total paw touches) during rearing in a cylinder (right). Data represented as box plots indicating 25th to 75th percentiles and median as the solid line with whiskers denoting minimum and maximum values. n = 9-14 mice per condition.

The *p* values were calculated by one-way ANOVA followed by Tukey's post hoc test. $*p < 0.05$, $**p < 0.01$, $***p < 0.001$, $****p < 0.0001$.

Figure 4: Intra-striatal administration of AiE0450h-AADC-HA reduced L-DOPA-induced dyskinesia (LID) in 6-OHDA unilateral toxin model

(A) Schematic overview of the injections and the behavioral tests. 6-OHDA toxin was stereotactically injected into the right dorsal striatum of P70 mice. 3 weeks after the surgery, a series of behavioral tests were performed 45 mins after either saline or different doses of L-DOPA intraperitoneal injection as noted.

(B) Retention time of the mice in the accelerating rotarod test (left) and quantification of total distance traveled in the open field test (middle) (as percentage change from saline-injected, toxin-treated mice). Quantification of the net contralateral rotations in a cylinder over 10 mins (right). Data represented as mean ± SEM. n = 6-14 mice per condition. The *p* values were calculated by one-way ANOVA followed by Dunnett's post hoc test. $*p < 0.05$, $**p < 0.01$, $****p < 0.0001$.

(C) Schematic overview of the injections and the behavioral tests. 6-OHDA toxin was stereotactically injected into the right dorsal striatum of P70 mice. 3 weeks after the surgery, the viral vectors were administered bilaterally to the dorsal striatum, and intraperitoneal L-DOPA was administered daily for 2 weeks before testing dyskinesia (axial, limb, and orolingual).

(D) Quantification of L-DOPA induced dyskinesia (LID) as the cumulation occurrence of abnormal involuntary movements (AIMs) affecting axial, limb, and orolingual muscles (left) and net contralateral rotations (right) in a cylinder over 10 mins. Data represented as box plots indicating 25th to 75th percentiles and median as the solid line with whiskers denoting minimum and maximum values and as mean ± SEM for rotations. N = 6-13 mice per condition.

The *p* values were calculated by one-way ANOVA followed by Dunnett's post hoc test. $**p < 0.01$, $****p < 0.0001$.

Figure 5: AiE0450h-AADC-HA rescued specific motor behaviors in MCI-Park genetic model

(A) Schematic overview of the injections and the behavioral tests. Male MCI-Park (*Slc6a3*$^{+/cre}$; *Ndufs2*$^{fl/fl}$) and age-matched littermate controls (*Slc6a3*$^{+/+}$; *Ndufs2*$^{fl/fl}$) were RO injected with either the viral vectors or the vehicle at P30-35. 4 weeks later at around P60, a series of behavioral tests were performed 45 mins after L-DOPA intraperitoneal injection.

(B) Retention time of the male mice in the accelerating rotarod test (left) and quantification of total distance traveled in the open field test (right). Data represented as box plots indicating 25th to 75th percentiles and median as the solid line with whiskers denoting minimum and maximum values. n = 7-10 mice per condition. The *p* values were calculated by one-way ANOVA followed by Tukey's post hoc test. $*p < 0.05$, $**p < 0.01$, $***p < 0.001$, $****p < 0.0001$.

(C) Representative coronal images of striatum (AP = +0.26 from bregma, top panel) for AiE0450h-AADC-HA showing AADC-HA (green) (top panel), midbrain (AP = -3.16 from bregma, middle panel) and LC (AP = -5.40 from bregma, bottom panel), following RO administration. Low magnification (10X) stitched, scale bars, 500 μm, top; High magnification (20X), scale bars, 20 μm as insets.

(D) Schematic overview of the injections and the behavioral tests. Female MCI-Park (*Slc6a3*$^{+/cre}$; *Ndufs2*$^{fl/fl}$) and age-matched littermate controls (*Slc6a3*$^{+/+}$; *Ndufs2*$^{fl/fl}$) were RO injected with either the viral vectors or the vehicle at P30-35. 4 weeks later at around P60, a series of behavioral tests were performed 45 mins after L-DOPA intraperitoneal injection at the doses mentioned.

(E) Retention time of the female mice in the accelerating rotarod test (left) and quantification of total distance traveled in the open field test (right). Data represented as box plots indicating 25th to 75th percentiles and median as the solid line with whiskers denoting minimum and maximum values. n = 9 mice per condition. The *p* values were calculated by one-way ANOVA followed by Tukey's post hoc test. $*p < 0.05$, $**p < 0.01$, $***p < 0.001$, $****p < 0.0001$.

(F) Representative coronal images of striatum (AP = +0.26 from bregma, top panel) for AiE0450h-AADC-HA showing AADC-HA (green) (top panel), midbrain (AP= -3.16 from bregma,

middle panel) and LC (AP= -5.40 from bregma, bottom panel) showing AADC-HA (green), following RO administration. Low magnification (10X) stitched, scale bars, 500 μm, top; High magnification (20X), scale bars, 20 μm as insets.

(G) Schematic overview of the injections and the behavioral tests. The viral vectors or the vehicle was bilaterally injected into the dorsal striatum of male MCI-Park (*Slc6a3*$^{+/cre}$; *Ndufs2*$^{fl/fl}$) and age-matched littermate controls (*Slc6a3*$^{+/+}$; *Ndufs2*$^{fl/fl}$) at P30-35. 4 weeks later at around P60, a series of behavioral tests were performed 45 mins after L-DOPA intraperitoneal injection.

(H) Retention time of the mice in the accelerating rotarod test (left) and quantification of total distance traveled in the open field test (right). Data represented as box plots indicating 25th to 75th percentiles and median as the solid line with whiskers denoting minimum and maximum values. n = 5-9 mice per condition. The *p* values were calculated by one-way ANOVA followed by Dunnett's post hoc test. $*p < 0.05$, $****p < 0.0001$.

(I) Representative coronal images of striatum (AP = +0.14 from bregma) for AiE0450h-AADC-HA (top panel) and CMV-AADC-HA (bottom panel) showing AADC-HA (green). Low magnification (10X) stitched, scale bars, 500 μm.

Figure 6: Retroorbital administration of AADC in other relevant cell types differentially rescued specific motor behaviors in PD model

(A) Schematic showing the vector designs for AiE0743m_3xC2-AADC-HA, AiE0888m-AADC-HA, and AiE0387m_3xC1-AADC-HA.

(B) For AiE0743m_3xC2-AADC-HA: Representative images of striatal (AP = +0.14 to +0.26 from bregma) coronal images of AADC-HA (green) and Chat+ cells (magenta) in the left panel, midbrain (AP = -2.92 to -3.08 from bregma) coronal images of AADC-HA (green) and TH+ cells (red) in the middle panel, and LC (AP= -5.40 to -5.52 from bregma) coronal images of AADC-HA (green) and TH+ cells (red) in the right panel. Low magnification (10X) stitched, scale bars, 500 μm; High magnification (20X), scale bars, 10 μm for STR and 20 μm for VTA and LC. White arrows depict representative colocalized cells.

(C) For AiE0888m-AADC-HA: Representative images of striatal (AP = +0.14 to +0.26 from bregma) coronal images of AADC-HA (green) and DARPP-32+ MSNs (magenta) in the left panel, midbrain (AP = -2.92 to -3.08 from bregma) coronal images of AADC-HA (green) and TH+ cells (red) in the middle panel, and LC (AP = -5.40 to -5.52 from bregma) coronal images of AADC-HA (green) and TH+ cells (red) in the right panel. Low magnification (10X) stitched, scale bars, 500 μm; High magnification (20X), scale bars, 10 μm for STR and 20 μm for VTA and LC. White arrows depict representative colocalized cells.

(D) For AiE0387m_3xC1-AADC-HA: Representative images of striatal (AP = +0.14 to +0.26 from bregma) coronal images of AADC-HA (green) and GFAP+ cells (magenta) in the left panel, midbrain (AP = -2.92 to -3.08 from bregma) coronal images of AADC-HA (green) and TH+ cells (red) in the middle panel, and LC (AP = -5.40 to -5.52 from bregma) coronal images of AADC-HA (green) and TH+ cells (red) in the right panel. Low magnification (10X) stitched, scale bars, 500 μm; High magnification (20X), scale bars, 10 μm for STR and 20 μm for VTA and LC. White arrows depict representative colocalized cells.

(E) Schematic overview of the injections and the behavioral tests. 6-OHDA toxin was stereotactically injected into the right dorsal striatum of P70 mice. 3 weeks after the surgery, they received RO injection of the viral vectors, and a series of behavioral tests were performed 3 weeks later, 45 mins after L-DOPA intraperitoneal injection.

(F) Retention time of the mice in the accelerating rotarod test (left) and quantification of total distance traveled in the open field test (right). Data represented as box plots indicating 25th to 75th percentiles and median as the solid line with whiskers denoting minimum and maximum values. n = 21 (SYFP2 control), 8-14 (viral vectors). The *p* values were calculated by one-way ANOVA followed by Dunnett's post hoc test. $**p < 0.01$, $****p < 0.0001$.

(G) MCI-Park (*Slc6a3*$^{+/cre}$; *Ndufs2*$^{fl/fl}$) and age-matched littermate controls (*Slc6a3*$^{+/+}$; *Ndufs2*$^{fl/fl}$) were RO injected with the viral vectors at P30-35. 4 weeks later at around P60, a series of behavioral tests were performed 45 mins after L-DOPA intraperitoneal injection.

(H) Retention time of the mice in the accelerating rotarod test (left) and quantification of total distance traveled in the open field test (right). Data represented as box plots indicating 25th to 75th percentiles and median as the solid line with whiskers denoting minimum and maximum values. n = 10 (WT), 13-15 (viral vectors). The *p* values were calculated by one-way ANOVA followed by Dunnett's post hoc test. $*p < 0.05$, $****p < 0.0001$.

Figure 7: Intracerebroventricular (ICV) and intraparenchymal administration of AiE0450h-AADC-HA in non-human primates showed specific and robust expression of the therapeutic cargo

(A) Representative coronal images of AADC-HA (green) and DARPP-32+ MSNs (magenta) for AiE0450h-AADC-HA (left panel), in the cortex (top right panel) and in the caudate (bottom right panel), following ICV administration. (B) Representative coronal images of SYFP2 (green) and DARPP-32+ MSNs (magenta) for hSyn1-SYFP2-H2B (left panel, in the cortex (top right panel) and in the caudate (bottom right panel), following ICV administration. (C) Representative coronal images of AADC-HA (green) and DARPP-32+ MSNs (magenta) for AiE0450h-AADC-HA (left panel, in the cortex (top right panel) and in the caudate (bottom right panel), following intraparenchymal administration. Low magnification (4X) stitched, scale bars, 2000 μm; High magnification (20X), scale bars, 100 μm. White arrows depict representative colocalized cells. (D) Heatmap of specificities for AiE0450h-AADC-HA and hSyn1-SYFP2-H2B determined by IHC with AADC-HA and SYFP2 antibodies for the two vectors respectively colocalized to the cell-type marker DARPP-32+ for MSNs, following intracerebroventricular and intraparenchymal routes of administration. NA = not available. Legend with scale denotes values ranging from 0 (cyan) to 100% (magenta). Percentage values are the average mean value from 3 sections of n = 1 animal analyzed.

References:

1. Luo, Y., Qiao, L., Li, M., Wen, X., Zhang, W., and Li, X. (2025). Global, regional, national epidemiology and trends of Parkinson's disease from 1990 to 2021: findings from the Global Burden of Disease Study 2021. Front. Aging Neurosci. *16*, 1498756. https://doi.org/10.3389/fnagi.2024.1498756.
2. Yang, W., Hamilton, J.L., Kopil, C., Beck, J.C., Tanner, C.M., Albin, R.L., Ray Dorsey, E., Dahodwala, N., Cintina, I., Hogan, P., et al. (2020). Current and projected future economic burden of Parkinson's disease in the U.S. npj Parkinsons Dis. *6*, 15. https://doi.org/10.1038/s41531-020-0117-1.
3. Moustafa, A.A., Chakravarthy, S., Phillips, J.R., Gupta, A., Keri, S., Polner, B., Frank, M.J., and Jahanshahi, M. (2016). Motor symptoms in Parkinson's disease: A unified framework. Neuroscience & Biobehavioral Reviews *68*, 727–740. https://doi.org/10.1016/j.neubiorev.2016.07.010.
4. Jankovic, J. (2008). Parkinson's disease: clinical features and diagnosis. J Neurol Neurosurg Psychiatry *79*, 368. https://doi.org/10.1136/jnnp.2007.131045.
5. DeLong, M.R., and Wichmann, T. (2007). Circuits and Circuit Disorders of the Basal Ganglia. Arch Neurol *64*, 20. https://doi.org/10.1001/archneur.64.1.20.
6. Zhou, Z.D., Yi, L.X., Wang, D.Q., Lim, T.M., and Tan, E.K. (2023). Role of dopamine in the pathophysiology of Parkinson's disease. Transl Neurodegener *12*, 44. https://doi.org/10.1186/s40035-023-00378-6.
7. Luk, K.C., Kehm, V., Carroll, J., Zhang, B., O'Brien, P., Trojanowski, J.Q., and Lee, V.M.-Y. (2012). Pathological α-Synuclein Transmission Initiates Parkinson-like Neurodegeneration in Nontransgenic Mice. Science *338*, 949–953. https://doi.org/10.1126/science.1227157.
8. Lundblad, M., Picconi, B., Lindgren, H., and Cenci, M.A. (2004). A model of l-DOPA-induced dyskinesia in 6-hydroxydopamine lesioned mice: relation to motor and cellular parameters of

nigrostriatal function. Neurobiology of Disease *16*, 110–123. https://doi.org/10.1016/j.nbd.2004.01.007.

9. Dwi Wahyu, I., Chiken, S., Hasegawa, T., Sano, H., and Nambu, A. (2021). Abnormal Cortico-Basal Ganglia Neurotransmission in a Mouse Model of l-DOPA-Induced Dyskinesia. J. Neurosci. *41*, 2668–2683. https://doi.org/10.1523/JNEUROSCI.0267-20.2020.
10. Lundblad, M., Usiello, A., Carta, M., Håkansson, K., Fisone, G., and Cenci, M.A. (2005). Pharmacological validation of a mouse model of l-DOPA-induced dyskinesia. Experimental Neurology *194*, 66–75. https://doi.org/10.1016/j.expneurol.2005.02.002.
11. Yang, K., Zhao, X., Wang, C., Zeng, C., Luo, Y., and Sun, T. (2021). Circuit Mechanisms of L-DOPA-Induced Dyskinesia (LID). Front. Neurosci. *15*, 614412. https://doi.org/10.3389/fnins.2021.614412.
12. García-González, N., Gonçalves-Sánchez, J., Gómez-Nieto, R., Gonçalves-Estella, J.M., and López, D.E. (2024). Advances and Challenges in Gene Therapy for Neurodegenerative Diseases: A Systematic Review. IJMS *25*, 12485. https://doi.org/10.3390/ijms252312485.
13. Liu, F., Li, R., Zhu, Z., Yang, Y., and Lu, F. (2024). Current developments of gene therapy in human diseases. MedComm *5*, e645. https://doi.org/10.1002/mco2.645.
14. Ogbonmide, T., Rathore, R., Rangrej, S.B., Hutchinson, S., Lewis, M., Ojilere, S., Carvalho, V., and Kelly, I. (2023). Gene Therapy for Spinal Muscular Atrophy (SMA): A Review of Current Challenges and Safety Considerations for Onasemnogene Abeparvovec (Zolgensma). Cureus. https://doi.org/10.7759/cureus.36197.
15. Reape, K.Z., and High, K.A. (2023). Trial by “Firsts”: Clinical Trial Design and Regulatory Considerations in the Development and Approval of the First AAV Gene Therapy Product in the United States. Cold Spring Harb Perspect Med *13*, a041312. https://doi.org/10.1101/cshperspect.a041312.

16. Naso, M.F., Tomkowicz, B., Perry, W.L., and Strohl, W.R. (2017). Adeno-Associated Virus (AAV) as a Vector for Gene Therapy. BioDrugs *31*, 317–334. https://doi.org/10.1007/s40259-017-0234-5.

17. Byrne, B.J., Flanigan, K.M., Matesanz, S.E., Finkel, R.S., Waldrop, M.A., D'Ambrosio, E.S., Johnson, N.E., Smith, B.K., Bönnemann, C., Carrig, S., et al. (2025). Current clinical applications of AAV-mediated gene therapy. Molecular Therapy *33*, 2479–2516. https://doi.org/10.1016/j.ymthe.2025.04.045.

18. Merola, A., Kobayashi, N., Romagnolo, A., Wright, B.A., Artusi, C.A., Imbalzano, G., Litvan, I., Van Laar, A.D., and Bankiewicz, K. (2021). Gene Therapy in Movement Disorders: A Systematic Review of Ongoing and Completed Clinical Trials. Front. Neurol. *12*, 648532. https://doi.org/10.3389/fneur.2021.648532.

19. Zhu, M.Y., Juorio, A.V., Paterson, I.A., and Boulton, A.A. (1992). Regulation of Aromatic L-Amino Acid Decarboxylase by Dopamine Receptors in the Rat Brain. Journal of Neurochemistry *58*, 636–641. https://doi.org/10.1111/j.1471-4159.1992.tb09765.x.

20. Chien, Y.-H., Lee, N.-C., Tseng, S.-H., Tai, C.-H., Muramatsu, S., Byrne, B.J., and Hwu, W.-L. (2017). Efficacy and safety of AAV2 gene therapy in children with aromatic L-amino acid decarboxylase deficiency: an open-label, phase 1/2 trial. The Lancet Child & Adolescent Health *1*, 265–273. https://doi.org/10.1016/S2352-4642(17)30125-6.

21. Kojima, K., Nakajima, T., Taga, N., Miyauchi, A., Kato, M., Matsumoto, A., Ikeda, T., Nakamura, K., Kubota, T., Mizukami, H., et al. (2019). Gene therapy improves motor and mental function of aromatic l-amino acid decarboxylase deficiency. Brain *142*, 322–333. https://doi.org/10.1093/brain/awy331.

22. Upstaza™ Granted Marketing Authorization by European Commission as First Disease-Modifying Treatment for AADC Deficiency.

23. Sánchez-Pernaute, R., Harvey-White, J., Cunningham, J., and Bankiewicz, K.S. (2001). Functional Effect of Adeno-associated Virus Mediated Gene Transfer of Aromatic L-Amino

Acid Decarboxylase into the Striatum of 6-OHDA-Lesioned Rats. Molecular Therapy *4*, 324–330. https://doi.org/10.1006/mthe.2001.0466.

24. Nutt, J.G., Curtze, C., Hiller, A., Anderson, S., Larson, P.S., Van Laar, A.D., Richardson, R.M., Thompson, M.E., Sedkov, A., Leinonen, M., et al. (2020). Aromatic L-Amino Acid Decarboxylase Gene Therapy Enhances Levodopa Response in Parkinson's Disease. Movement Disorders *35*, 851–858. https://doi.org/10.1002/mds.27993.

25. Hadaczek, P., Eberling, J.L., Pivirotto, P., Bringas, J., Forsayeth, J., and Bankiewicz, K.S. (2010). Eight Years of Clinical Improvement in MPTP-Lesioned Primates After Gene Therapy With AAV2-hAADC. Molecular Therapy *18*, 1458–1461. https://doi.org/10.1038/mt.2010.106.

26. Hwu, P.W., Kiening, K., Anselm, I., Compton, D.R., Nakajima, T., Opladen, T., Pearl, P.L., Roubertie, A., Roujeau, T., and Muramatsu, S. (2021). Gene therapy in the putamen for curing AADC deficiency and Parkinson's disease. EMBO Mol Med *13*, e14712. https://doi.org/10.15252/emmm.202114712.

27. Cunningham, J., Pivirotto, P., Bringas, J., Suzuki, B., Vijay, S., Sanftner, L., Kitamura, M., Chan, C., and Bankiewicz, K.S. (2008). Biodistribution of Adeno-associated Virus Type-2 in Nonhuman Primates after Convection-enhanced Delivery to Brain. Molecular Therapy *16*, 1267–1275. https://doi.org/10.1038/mt.2008.111.

28. Sanftner, L.M., Suzuki, B.M., Doroudchi, M.M., Feng, L., McClelland, A., Forsayeth, J.R., and Cunningham, J. (2004). Striatal Delivery of rAAV-hAADC to Rats with Preexisting Immunity to AAV. Molecular Therapy *9*, 403–409. https://doi.org/10.1016/j.ymthe.2003.12.005.

29. Christine, C.W., Bankiewicz, K.S., Van Laar, A.D., Richardson, R.M., Ravina, B., Kells, A.P., Boot, B., Martin, A.J., Nutt, J., Thompson, M.E., et al. (2019). Magnetic resonance imaging–guided phase 1 trial of putaminal *AADC* gene therapy for Parkinson's disease. Annals of Neurology *85*, 704–714. https://doi.org/10.1002/ana.25450.

30. Mittermeyer, G., Christine, C.W., Rosenbluth, K.H., Baker, S.L., Starr, P., Larson, P., Kaplan, P.L., Forsayeth, J., Aminoff, M.J., and Bankiewicz, K.S. (2012). Long-Term Evaluation of a Phase 1 Study of AADC Gene Therapy for Parkinson's Disease. Human Gene Therapy *23*, 377–381. https://doi.org/10.1089/hum.2011.220.

31. Christine, C.W., Richardson, R.M., Van Laar, A.D., Thompson, M.E., Fine, E.M., Khwaja, O.S., Li, C., Liang, G.S., Meier, A., Roberts, E.W., et al. (2022). Safety of AADC Gene Therapy for Moderately Advanced Parkinson Disease: Three-Year Outcomes From the PD-1101 Trial. Neurology *98*. https://doi.org/10.1212/WNL.0000000000012952.

32. Daci, R., and Flotte, T.R. (2024). Delivery of Adeno-Associated Virus Vectors to the Central Nervous System for Correction of Single Gene Disorders. IJMS *25*, 1050. https://doi.org/10.3390/ijms25021050.

33. Chan, K.Y., Jang, M.J., Yoo, B.B., Greenbaum, A., Ravi, N., Wu, W.-L., Sánchez-Guardado, L., Lois, C., Mazmanian, S.K., Deverman, B.E., et al. (2017). Engineered AAVs for efficient noninvasive gene delivery to the central and peripheral nervous systems. Nat Neurosci *20*, 1172–1179. https://doi.org/10.1038/nn.4593.

34. Morabito, G., Giannelli, S.G., Ordazzo, G., Bido, S., Castoldi, V., Indrigo, M., Cabassi, T., Cattaneo, S., Luoni, M., Cancellieri, C., et al. (2017). AAV-PHP.B-Mediated Global-Scale Expression in the Mouse Nervous System Enables GBA1 Gene Therapy for Wide Protection from Synucleinopathy. Molecular Therapy *25*, 2727–2742. https://doi.org/10.1016/j.ymthe.2017.08.004.

35. Ressler, R., McDowell, K., Wheeler, B., Thomas, S., Grigoryeva, L., Armendariz, A., Flynn, M., Acharya, H., Denis, P., Tchourilov, P., et al. (2025). Systemic AAV Gene Therapy Using a CNS-targeted Engineered Capsid Significantly Increases GCase Activity to Support the Potential Treatment of PD-GBA (S37.007). Neurology *104*, 5149. https://doi.org/10.1212/WNL.0000000000212169.

36. Huang, Q., Chan, K.Y., Wu, J., Botticello-Romero, N.R., Zheng, Q., Lou, S., Keyes, C., Svanbergsson, A., Johnston, J., Mills, A., et al. (2024). An AAV capsid reprogrammed to bind human transferrin receptor mediates brain-wide gene delivery. Science *384*, 1220–1227. https://doi.org/10.1126/science.adm8386.

37. Moyer, T.C., Hoffman, B.A., Chen, W., Shah, I., Ren, X.-Q., Knox, T., Liu, J., Wang, W., Li, J., Khalid, H., et al. (2025). Highly conserved brain vascular receptor ALPL mediates transport of engineered AAV vectors across the blood-brain barrier. Molecular Therapy *33*, 3902–3916. https://doi.org/10.1016/j.ymthe.2025.04.046.

38. Szunyogh, S., Carroll, E., and Wade-Martins, R. (2025). Recent developments in gene therapy for Parkinson's disease. Molecular Therapy *33*, 2052–2064. https://doi.org/10.1016/j.ymthe.2025.03.030.

39. Graybuck, L.T., Daigle, T.L., Sedeño-Cortés, A.E., Walker, M., Kalmbach, B., Lenz, G.H., Morin, E., Nguyen, T.N., Garren, E., Bendrick, J.L., et al. (2021). Enhancer viruses for combinatorial cell-subclass-specific labeling. Neuron *109*, 1449-1464.e13. https://doi.org/10.1016/j.neuron.2021.03.011.

40. Hunker, A.C., Wirthlin, M.E., Gill, G., Johansen, N.J., Hooper, M., Omstead, V., Vargas, S., Lerma, M.N., Taskin, N., Weed, N., et al. (2025). Enhancer AAV toolbox for accessing and perturbing striatal cell types and circuits. Neuron *113*, 1507-1524.e17. https://doi.org/10.1016/j.neuron.2025.04.035.

41. Kussick, E., Johansen, N., Taskin, N., Chowdhury, A., Quinlan, M.A., Fraser, A., Clark, A.G., Wynalda, B., Martinez, R., Groce, E.L., et al. (2025). Enhancer AAVs for targeting spinal motor neurons and descending motor pathways in rodents and macaque. Cell Reports *44*, 115730. https://doi.org/10.1016/j.celrep.2025.115730.

42. Mich, J.K., Graybuck, L.T., Hess, E.E., Mahoney, J.T., Kojima, Y., Ding, Y., Somasundaram, S., Miller, J.A., Kalmbach, B.E., Radaelli, C., et al. (2021). Functional

enhancer elements drive subclass-selective expression from mouse to primate neocortex. Cell Reports *34*, 108754. https://doi.org/10.1016/j.celrep.2021.108754.

43. Ben-Simon, Y., Hooper, M., Narayan, S., Daigle, T.L., Dwivedi, D., Way, S.W., Oster, A., Stafford, D.A., Mich, J.K., Taormina, M.J., et al. (2025). A suite of enhancer AAVs and transgenic mouse lines for genetic access to cortical cell types. Cell *188*, 3045-3064.e23. https://doi.org/10.1016/j.cell.2025.05.002.

44. Mich, J.K., Ryu, J., Wei, A.D., Gore, B.B., Guo, R., Bard, A.M., Martinez, R.A., Luber, E.M., Liu, J., Bishaw, Y.M., et al. (2025). Interneuron-specific dual-AAV *SCN1A* gene replacement corrects epileptic phenotypes in mouse models of Dravet syndrome. Sci. Transl. Med. *17*, eadn5603. https://doi.org/10.1126/scitranslmed.adn5603.

45. Quinlan, M.A., Guo, R., Clark, A.G., Luber, E.M., Christian, R.J., Martinez, R.A., Groce, E.L., Liu, J., Bishaw, Y.M., Bhowmik, R., et al. (2025). AAV delivery of full-length SYNGAP1 rescues epileptic and behavioral phenotypes in a mouse model of SYNGAP1-related disorders. Molecular Therapy, S1525001625007592. https://doi.org/10.1016/j.ymthe.2025.09.040.

46. Lee, H., Weinberg-Wolf, H., Lee, H.-L., Lee, T., Conte, J., Godoy-Parejo, C., Demb, J.B., Rudenko, A., and Kim, I.-J. (2023). Brn3b regulates the formation of fear-related midbrain circuits and defensive responses to visual threat. PLoS Biol *21*, e3002386. https://doi.org/10.1371/journal.pbio.3002386.

47. Xu, D., Wang, X., Jia, Y., Wang, T., Tian, Z., Feng, X., and Zhang, Y. (2018). SV40 intron, a potent strong intron element that effectively increases transgene expression in transfected Chinese hamster ovary cells. J Cellular Molecular Medi *22*, 2231–2239. https://doi.org/10.1111/jcmm.13504.

48. Ivkovic, S., and Ehrlich, M.E. (1999). Expression of the Striatal DARPP-32/ARPP-21 Phenotype in GABAergic Neurons Requires Neurotrophins *In Vivo* and *In Vitro*. J. Neurosci. *19*, 5409–5419. https://doi.org/10.1523/JNEUROSCI.19-13-05409.1999.

49. Fu, Y., Paxinos, G., Watson, C., and Halliday, G.M. (2016). The substantia nigra and ventral tegmental dopaminergic neurons from development to degeneration. Journal of Chemical Neuroanatomy *76*, 98–107. https://doi.org/10.1016/j.jchemneu.2016.02.001.

50. Bucci, D., Busceti, C.L., Calierno, M.T., Di Pietro, P., Madonna, M., Biagioni, F., Ryskalin, L., Limanaqi, F., Nicoletti, F., and Fornai, F. (2017). Systematic Morphometry of Catecholamine Nuclei in the Brainstem. Front. Neuroanat. *11*, 98. https://doi.org/10.3389/fnana.2017.00098.

51. Alvarez-Fischer, D., Henze, C., Strenzke, C., Westrich, J., Ferger, B., Höglinger, G.U., Oertel, W.H., and Hartmann, A. (2008). Characterization of the striatal 6-OHDA model of Parkinson's disease in wild type and α-synuclein-deleted mice. Experimental Neurology *210*, 182–193. https://doi.org/10.1016/j.expneurol.2007.10.012.

52. Stott, S.R.W., and Barker, R.A. (2014). Time course of dopamine neuron loss and glial response in the 6- OHDA striatal mouse model of P arkinson's disease. Eur J of Neuroscience *39*, 1042–1056. https://doi.org/10.1111/ejn.12459.

53. Mendes-Pinheiro, B., Soares-Cunha, C., Marote, A., Loureiro-Campos, E., Campos, J., Barata-Antunes, S., Monteiro-Fernandes, D., Santos, D., Duarte-Silva, S., Pinto, L., et al. (2021). Unilateral Intrastriatal 6-Hydroxydopamine Lesion in Mice: A Closer Look into Non-Motor Phenotype and Glial Response. IJMS *22*, 11530. https://doi.org/10.3390/ijms222111530.

54. Yu, C., Jiang, T.T., Shoemaker, C.T., Fan, D., Rossi, M.A., and Yin, H.H. (2022). Striatal mechanisms of turning behaviour following unilateral dopamine depletion in mice. Eur J of Neuroscience *56*, 4529–4545. https://doi.org/10.1111/ejn.15764.

55. Iancu, R., Mohapel, P., Brundin, P., and Paul, G. (2005). Behavioral characterization of a unilateral 6-OHDA-lesion model of Parkinson's disease in mice. Behavioural Brain Research *162*, 1–10. https://doi.org/10.1016/j.bbr.2005.02.023.

56. Sebastianutto, I., Maslava, N., Hopkins, C.R., and Cenci, M.A. (2016). Validation of an improved scale for rating l-DOPA-induced dyskinesia in the mouse and effects of specific dopamine receptor antagonists. Neurobiology of Disease *96*, 156–170. https://doi.org/10.1016/j.nbd.2016.09.001.

57. Fox, S.H., and Brotchie, J.M. (2010). The MPTP-lesioned non-human primate models of Parkinson's disease. Past, present, and future. In Progress in Brain Research (Elsevier), pp. 133–157. https://doi.org/10.1016/S0079-6123(10)84007-5.

58. Fabbrini, G., Brotchie, J.M., Grandas, F., Nomoto, M., and Goetz, C.G. (2007). Levodopa-induced dyskinesias. Movement Disorders *22*, 1379–1389. https://doi.org/10.1002/mds.21475.

59. Bastide, M.F., Meissner, W.G., Picconi, B., Fasano, S., Fernagut, P.-O., Feyder, M., Francardo, V., Alcacer, C., Ding, Y., Brambilla, R., et al. (2015). Pathophysiology of L-dopa-induced motor and non-motor complications in Parkinson's disease. Progress in Neurobiology *132*, 96–168. https://doi.org/10.1016/j.pneurobio.2015.07.002.

60. Ungerstedt, U. (1971). Postsynaptic Supersensitivity after 6-Hydroxy-dopamine Induced Degeneration of the Nigro-striatal Dopamine System. Acta Physiologica Scandinavica *82*, 69–93. https://doi.org/10.1111/j.1365-201X.1971.tb11000.x.

61. González-Rodríguez, P., Zampese, E., Stout, K.A., Guzman, J.N., Ilijic, E., Yang, B., Tkatch, T., Stavarache, M.A., Wokosin, D.L., Gao, L., et al. (2021). Disruption of mitochondrial complex I induces progressive parkinsonism. Nature *599*, 650–656. https://doi.org/10.1038/s41586-021-04059-0.

62. Mich, J.K., Sunil, S., Johansen, N., Martinez, R.A., Liu, J., Gore, B.B., Mahoney, J.T., Leytze, M., Ben-Simon, Y., Bertagnolli, D., et al. (2023). Enhancer-AAVs allow genetic access to oligodendrocytes and diverse populations of astrocytes across species. Preprint at Neuroscience, https://doi.org/10.1101/2023.09.20.558718 https://doi.org/10.1101/2023.09.20.558718.

63. Ichikawa, T., Ajiki, K., Matsuura, J., and Misawa, H. (1997). Localization of two cholinergic markers, choline acetyltransferase and vesicular acetylcholine transporter in the central nervous system of the rat: in situ hybridization histochemistry and immunohistochemistry. Journal of Chemical Neuroanatomy *13*, 23–39. https://doi.org/10.1016/S0891-0618(97)00021-5.

64. Hol, E.M., and Pekny, M. (2015). Glial fibrillary acidic protein (GFAP) and the astrocyte intermediate filament system in diseases of the central nervous system. Current Opinion in Cell Biology *32*, 121–130. https://doi.org/10.1016/j.ceb.2015.02.004.

65. Christine, C.W., Starr, P.A., Larson, P.S., Eberling, J.L., Jagust, W.J., Hawkins, R.A., VanBrocklin, H.F., Wright, J.F., Bankiewicz, K.S., and Aminoff, M.J. (2009). Safety and tolerability of putaminal *AADC* gene therapy for Parkinson disease. Neurology *73*, 1662–1669. https://doi.org/10.1212/WNL.0b013e3181c29356.

66. Sánchez-Pernaute, R., Harvey-White, J., Cunningham, J., and Bankiewicz, K.S. (2001). Functional Effect of Adeno-associated Virus Mediated Gene Transfer of Aromatic L-Amino Acid Decarboxylase into the Striatum of 6-OHDA-Lesioned Rats. Molecular Therapy *4*, 324–330. https://doi.org/10.1006/mthe.2001.0466.

67. Lee, N.-C., Muramatsu, S.-I., Chien, Y.-H., Liu, W.-S., Wang, W.-H., Cheng, C.-H., Hu, M.-K., Chen, P.-W., Tzen, K.-Y., Byrne, B.J., et al. (2015). Benefits of Neuronal Preferential Systemic Gene Therapy for Neurotransmitter Deficiency. Molecular Therapy *23*, 1572–1581. https://doi.org/10.1038/mt.2015.122.

68. Ikemoto, S., Yang, C., and Tan, A. (2015). Basal ganglia circuit loops, dopamine and motivation: A review and enquiry. Behavioural Brain Research *290*, 17–31. https://doi.org/10.1016/j.bbr.2015.04.018.

69. Graybiel, A.M. (2025). Surprises From the Basal Ganglia: Stop and Go Have New Meaning. Movement Disorders, mds.70008. https://doi.org/10.1002/mds.70008.

70. Ferrucci, M., S. Giorgi, F., Bartalucci, A., L. Busceti, C., and Fornai, F. (2013). The Effects of Locus Coeruleus and Norepinephrine in Methamphetamine Toxicity. Current Neuropharmacology *11*, 80–94. https://doi.org/10.2174/157015913804999522.

71. Zerbi, V., Floriou-Servou, A., Markicevic, M., Vermeiren, Y., Sturman, O., Privitera, M., Von Ziegler, L., Ferrari, K.D., Weber, B., De Deyn, P.P., et al. (2019). Rapid Reconfiguration of the Functional Connectome after Chemogenetic Locus Coeruleus Activation. Neuron *103*, 702-718.e5. https://doi.org/10.1016/j.neuron.2019.05.034.

72. Muramatsu, S., Fujimoto, K., Kato, S., Mizukami, H., Asari, S., Ikeguchi, K., Kawakami, T., Urabe, M., Kume, A., Sato, T., et al. (2010). A Phase I Study of Aromatic L-Amino Acid Decarboxylase Gene Therapy for Parkinson's Disease. Molecular Therapy *18*, 1731–1735. https://doi.org/10.1038/mt.2010.135.

73. Levodopa and the Progression of Parkinson's Disease (2004). N Engl J Med *351*, 2498–2508. https://doi.org/10.1056/NEJMoa033447.

74. Ahlskog, J.E., and Muenter, M.D. (2001). Frequency of levodopa-related dyskinesias and motor fluctuations as estimated from the cumulative literature. Movement Disorders *16*, 448–458. https://doi.org/10.1002/mds.1090.

75. Kwon, D.K., Kwatra, M., Wang, J., and Ko, H.S. (2022). Levodopa-Induced Dyskinesia in Parkinson's Disease: Pathogenesis and Emerging Treatment Strategies. Cells *11*, 3736. https://doi.org/10.3390/cells11233736.

76. Nyholm, D., Odin, P., Johansson, A., Chatamra, K., Locke, C., Dutta, S., and Othman, A.A. (2013). Pharmacokinetics of Levodopa, Carbidopa, and 3-O-Methyldopa Following 16-hour Jejunal Infusion of Levodopa-Carbidopa Intestinal Gel in Advanced Parkinson's Disease Patients. AAPS J *15*, 316–323. https://doi.org/10.1208/s12248-012-9439-1.

77. Bravi, D., Mouradian, M.M., Roberts, J.W., Davis, T.L., Sohn, Y.H., and Chase, T.N. (1994). Wearing-off fluctuations in Parkinson's disease: Contribution of postsynaptic mechanisms. Annals of Neurology *36*, 27–31. https://doi.org/10.1002/ana.410360108.

78. Jenner, P. (2008). Molecular mechanisms of L-DOPA-induced dyskinesia. Nat Rev Neurosci *9*, 665–677. https://doi.org/10.1038/nrn2471.

79. Picconi, B., Centonze, D., Håkansson, K., Bernardi, G., Greengard, P., Fisone, G., Cenci, M.A., and Calabresi, P. (2003). Loss of bidirectional striatal synaptic plasticity in L-DOPA–induced dyskinesia. Nat Neurosci *6*, 501–506. https://doi.org/10.1038/nn1040.

80. Hauser, R.A., Torres-Yaghi, Y., Fisher, S., and Banisadr, G. (2025). How to dose extended-release carbidopa-levodopa capsules (IPX203, CREXONT®) in patients with Parkinson's disease. Clinical Parkinsonism & Related Disorders *13*, 100357. https://doi.org/10.1016/j.prdoa.2025.100357.

81. Soileau, M.J., Aldred, J., Budur, K., Fisseha, N., Fung, V.S., Jeong, A., Kimber, T.E., Klos, K., Litvan, I., O'Neill, D., et al. (2022). Safety and efficacy of continuous subcutaneous foslevodopa-foscarbidopa in patients with advanced Parkinson's disease: a randomised, double-blind, active-controlled, phase 3 trial. The Lancet Neurology *21*, 1099–1109. https://doi.org/10.1016/S1474-4422(22)00400-8.

82. Aldred, J., Freire-Alvarez, E., Amelin, A.V., Antonini, A., Bergmans, B., Bergquist, F., Bouchard, M., Budur, K., Carroll, C., Chaudhuri, K.R., et al. (2023). Continuous Subcutaneous Foslevodopa/Foscarbidopa in Parkinson's Disease: Safety and Efficacy Results From a 12-Month, Single-Arm, Open-Label, Phase 3 Study. Neurol Ther *12*, 1937–1958. https://doi.org/10.1007/s40120-023-00533-1.

83. Michel, P.P., Hirsch, E.C., and Hunot, S. (2016). Understanding Dopaminergic Cell Death Pathways in Parkinson Disease. Neuron *90*, 675–691. https://doi.org/10.1016/j.neuron.2016.03.038.

84. Pearson, T.S., Gupta, N., San Sebastian, W., Imamura-Ching, J., Viehoever, A., Grijalvo-Perez, A., Fay, A.J., Seth, N., Lundy, S.M., Seo, Y., et al. (2021). Gene therapy for aromatic L-amino acid decarboxylase deficiency by MR-guided direct delivery of AAV2-AADC to

midbrain dopaminergic neurons. Nat Commun *12*, 4251. https://doi.org/10.1038/s41467-021-24524-8.

85. Concha-Marambio, L., Pritzkow, S., Shahnawaz, M., Farris, C.M., and Soto, C. (2023). Seed amplification assay for the detection of pathologic alpha-synuclein aggregates in cerebrospinal fluid. Nat Protoc *18*, 1179–1196. https://doi.org/10.1038/s41596-022-00787-3.

86. Wagner, S.K., Romero-Bascones, D., Cortina-Borja, M., Williamson, D.J., Struyven, R.R., Zhou, Y., Patel, S., Weil, R.S., Antoniades, C.A., Topol, E.J., et al. (2023). Retinal Optical Coherence Tomography Features Associated With Incident and Prevalent Parkinson Disease. Neurology *101*. https://doi.org/10.1212/WNL.0000000000207727.

87. Svetel, M., Marić, G., Božić, M., Lazić, U., Milovanović, A., Jakšić, J., Petrović, I., Dimitrijević, A., Knežević, M., and Pekmezović, T. (2025). Retinal Thickness in Patients with Parkinson's Disease and Dopa Responsive Dystonia—Is There Any Difference? Biomedicines *13*, 1227. https://doi.org/10.3390/biomedicines13051227.

88. Lim, S.A.O., Kang, U.J., and McGehee, D.S. (2014). Striatal cholinergic interneuron regulation and circuit effects. Front. Synaptic Neurosci. *6*. https://doi.org/10.3389/fnsyn.2014.00022.

89. McKinley, J.W., Shi, Z., Kawikova, I., Hur, M., Bamford, I.J., Sudarsana Devi, S.P., Vahedipour, A., Darvas, M., and Bamford, N.S. (2019). Dopamine Deficiency Reduces Striatal Cholinergic Interneuron Function in Models of Parkinson's Disease. Neuron *103*, 1056-1072.e6. https://doi.org/10.1016/j.neuron.2019.06.013.

90. Ztaou, S., Maurice, N., Camon, J., Guiraudie-Capraz, G., Kerkerian-Le Goff, L., Beurrier, C., Liberge, M., and Amalric, M. (2016). Involvement of Striatal Cholinergic Interneurons and M1 and M4 Muscarinic Receptors in Motor Symptoms of Parkinson's Disease. Journal of Neuroscience *36*, 9161–9172. https://doi.org/10.1523/JNEUROSCI.0873-16.2016.

91. Asanuma, M., Miyazaki, I., Murakami, S., Diaz-Corrales, F.J., and Ogawa, N. (2014). Striatal Astrocytes Act as a Reservoir for L-DOPA. PLoS ONE *9*, e106362. https://doi.org/10.1371/journal.pone.0106362.

92. Inyushin, M.Y., Huertas, A., Kucheryavykh, Y.V., Kucheryavykh, L.Y., Tsydzik, V., Sanabria, P., Eaton, M.J., Skatchkov, S.N., Rojas, L.V., and Wessinger, W.D. (2012). L-DOPA Uptake in Astrocytic Endfeet Enwrapping Blood Vessels in Rat Brain. Parkinson's Disease *2012*, 1–8. https://doi.org/10.1155/2012/321406.

93. Cerri, S., Mus, L., and Blandini, F. (2019). Parkinson's Disease in Women and Men: What's the Difference? Journal of Parkinson's Disease *9*, 501–515. https://doi.org/10.3233/JPD-191683.

94. Antzoulatos, E., Jakowec, M.W., Petzinger, G.M., and Wood, R.I. (2010). Sex differences in motor behavior in the MPTP mouse model of Parkinson's disease. Pharmacology Biochemistry and Behavior *95*, 466–472. https://doi.org/10.1016/j.pbb.2010.03.009.

95. Tranchevent, L.-C., Halder, R., and Glaab, E. (2023). Systems level analysis of sex-dependent gene expression changes in Parkinson's disease. npj Parkinsons Dis. *9*, 8. https://doi.org/10.1038/s41531-023-00446-8.

96. Schaffner, S.L., Tosefsky, K.N., Inskter, A.M., Appel-Cresswell, S., and Schulze-Hentrich, J.M. (2025). Sex and gender differences in the molecular etiology of Parkinson's disease: considerations for study design and data analysis. Biol Sex Differ *16*, 7. https://doi.org/10.1186/s13293-025-00692-w.

97. Cortese, M., Riise, T., Engeland, A., Ascherio, A., and Bjørnevik, K. (2018). Urate and the risk of Parkinson's disease in men and women. Parkinsonism & Related Disorders *52*, 76–82. https://doi.org/10.1016/j.parkreldis.2018.03.026.

98. Kent, A.P., Stern, G.M., and Webster, R.A. (1990). The effect of benserazide on the peripheral and central distribution and metabolism of levodopa after acute and chronic

administration in the rat. British J Pharmacology *100*, 743–748. https://doi.org/10.1111/j.1476-5381.1990.tb14085.x.

99. Florio, E., Serra, M., Lewis, R.G., Kramár, E., Freidberg, M., Wood, M., Morelli, M., and Borrelli, E. (2022). D2R signaling in striatal spiny neurons modulates L-DOPA induced dyskinesia. iScience *25*, 105263. https://doi.org/10.1016/j.isci.2022.105263.

100. Francardo, V., Recchia, A., Popovic, N., Andersson, D., Nissbrandt, H., and Cenci, M.A. (2011). Impact of the lesion procedure on the profiles of motor impairment and molecular responsiveness to L-DOPA in the 6-hydroxydopamine mouse model of Parkinson's disease. Neurobiology of Disease *42*, 327–340. https://doi.org/10.1016/j.nbd.2011.01.024.

101. Daigle, T.L., Wetsel, W.C., and Caron, M.G. (2011). Opposite function of dopamine D1 and *N* -methyl-D-aspartate receptors in striatal cannabinoid-mediated signaling. Eur J of Neuroscience *34*, 1378–1389. https://doi.org/10.1111/j.1460-9568.2011.07874.x.

Figure 1

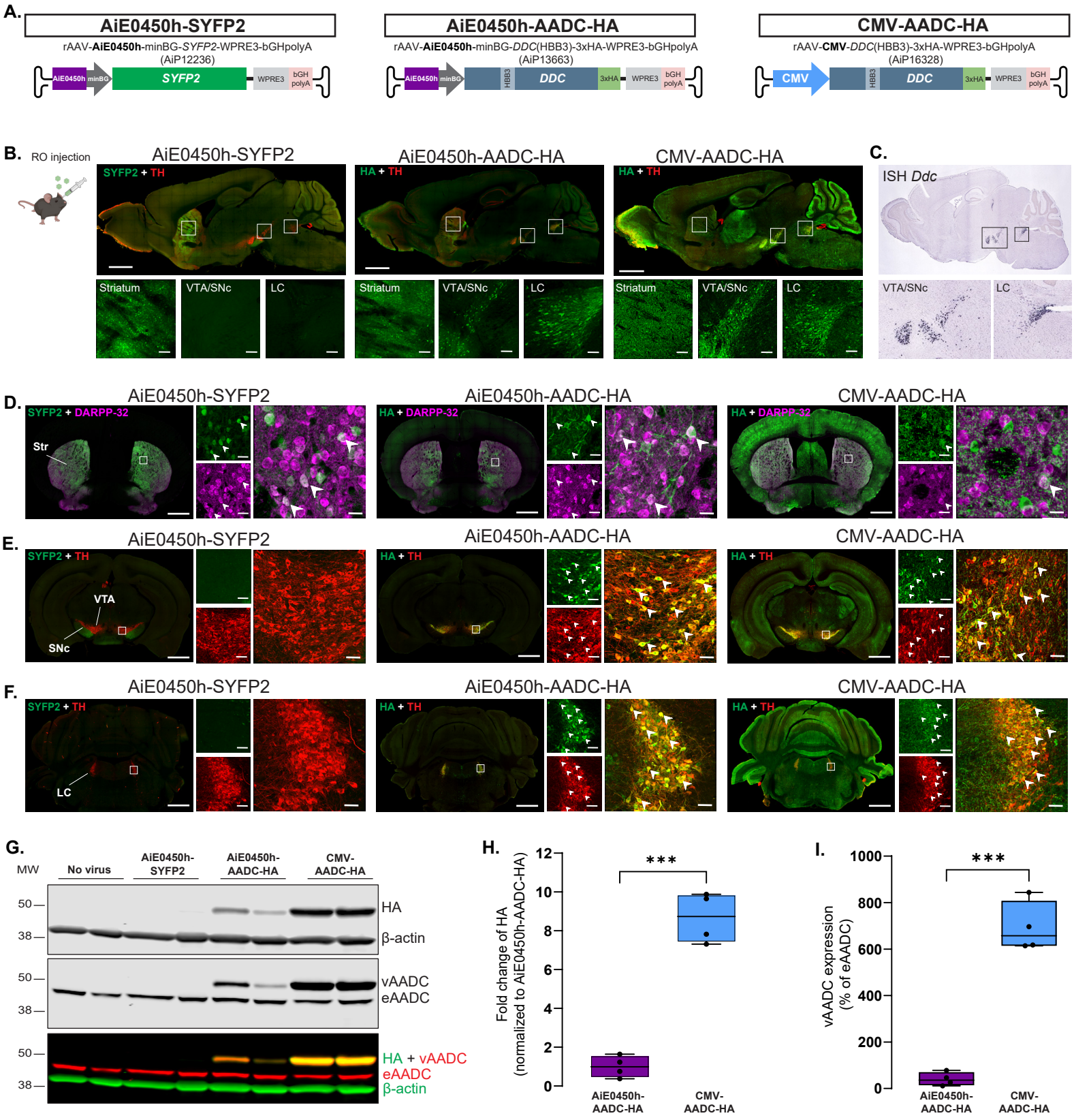
A.
AiE0450h-SYFP2
rAAV-AiE0450h-minBG-SYFP2-WPRE3-bGHpolyA
(AiP12236)
AiE0450h
minBG
SYFP2
WPRE3
bGH polyA
AiE0450h-AADC-HA
rAAV-AiE0450h-minBG-DDC(HBB3)-3xHA-WPRE3-bGHpolyA
(AiP13663)
HBB3
DDC
3xHA
CMV-AADC-HA
rAAV-CMV-DDC(HBB3)-3xHA-WPRE3-bGHpolyA
(AiP16328)
CMV
B.
RO injection
SYFP2 + TH
HA + TH
Striatum
VTA/SNc
LC
C.
ISH Ddc
D.
SYFP2 + DARPP-32
HA + DARPP-32
Str
E.
VTA
SNc
F.
LC
G.
MW
No virus
AiE0450h-SYFP2
AiE0450h-AADC-HA
CMV-AADC-HA
50
38
HA
β-actin
vAADC
eAADC
HA + vAADC
eAADC
β-actin
H.
Fold change of HA (normalized to AiE0450h-AADC-HA)
***
I.
vAADC expression (% of eAADC)
***

Figure 2

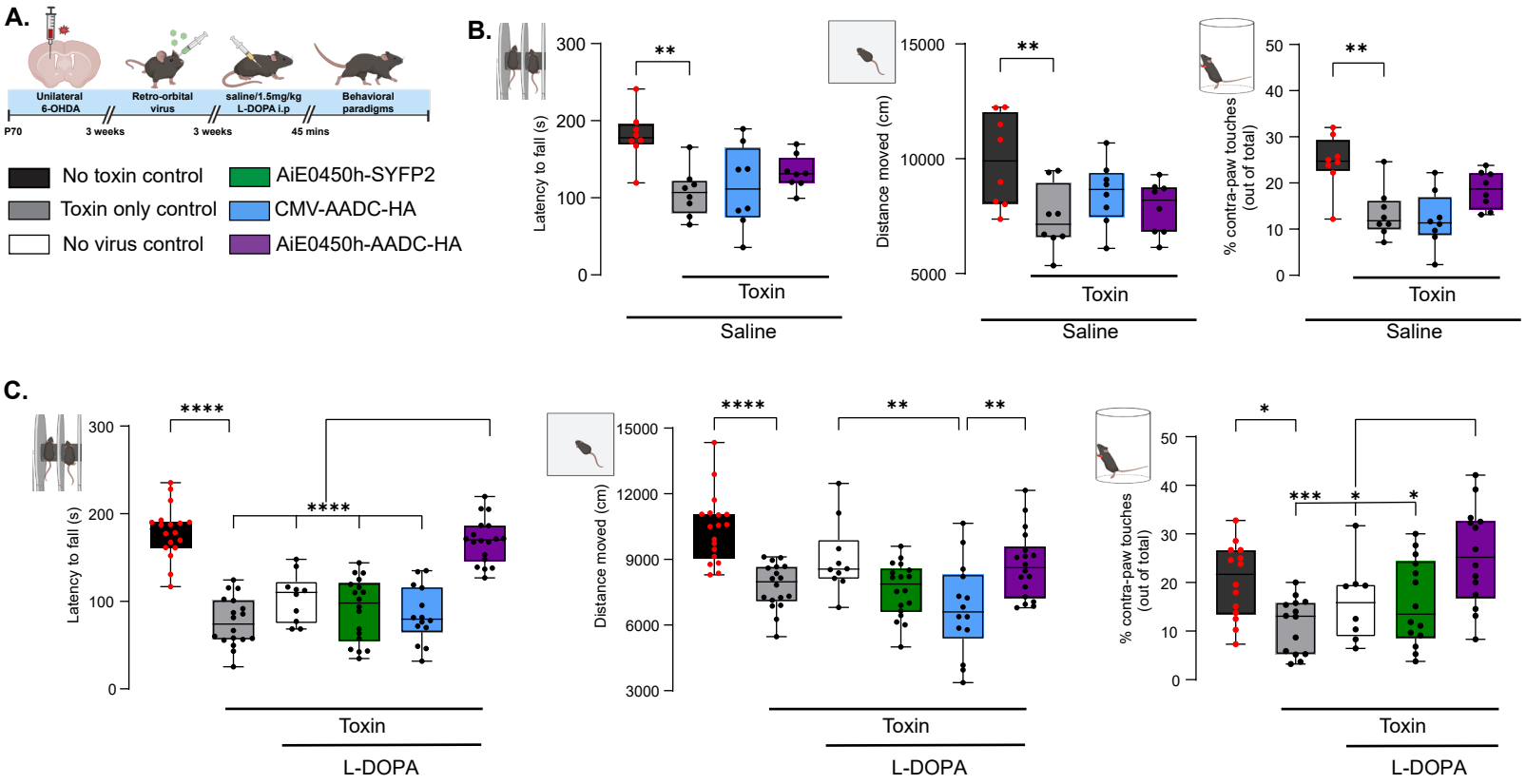
A.
Unilateral 6-OHDA
Retro-orbital virus
saline/1.5mg/kg L-DOPA i.p
Behavioral paradigms
P70
3 weeks
3 weeks
45 mins
No toxin control
Toxin only control
No virus control
AiE0450h-SYFP2
CMV-AADC-HA
AiE0450h-AADC-HA
B.
Latency to fall (s)
Distance moved (cm)
% contra-paw touches (out of total)
Toxin
Saline
C.
Latency to fall (s)
Distance moved (cm)
% contra-paw touches (out of total)
Toxin
L-DOPA

Figure 3

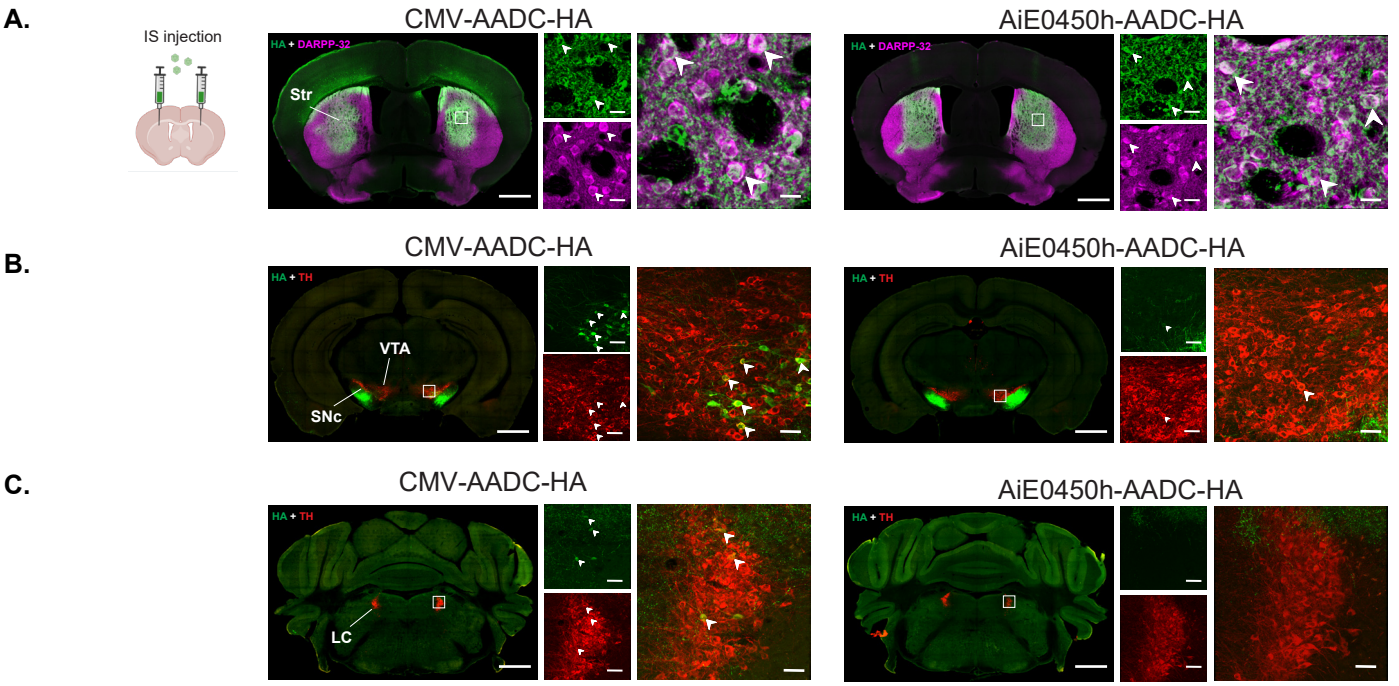
A.
IS injection
CMV-AADC-HA
AiE0450h-AADC-HA
HA + DARPP-32
Str
B.
HA + TH
VTA
SNc
C.
LC

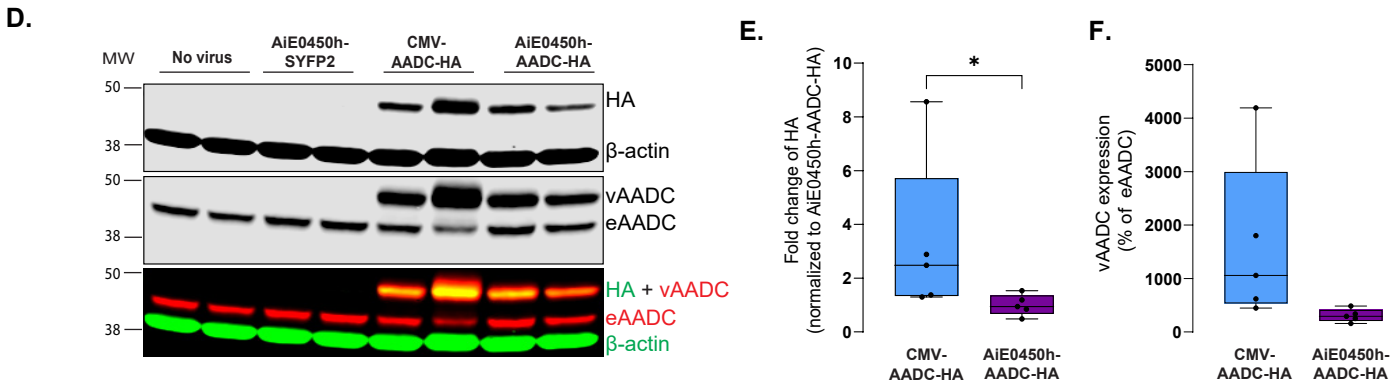
D.
MW
No virus
AiE0450h-SYFP2
CMV-AADC-HA
AiE0450h-AADC-HA
50
38
HA
β-actin
vAADC
eAADC
HA + vAADC
eAADC
β-actin
E.
Fold change of HA (normalized to AiE0450h-AADC-HA)
*
CMV-AADC-HA
AiE0450h-AADC-HA
F.
vAADC expression (% of eAADC)

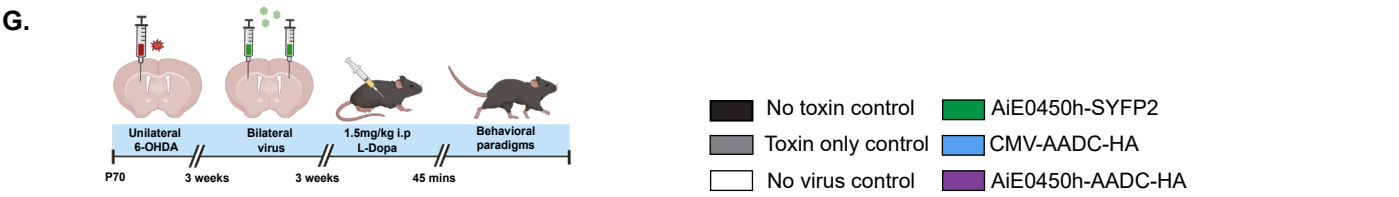
G.
Unilateral 6-OHDA
Bilateral virus
1.5mg/kg i.p L-Dopa
Behavioral paradigms
P70
3 weeks
3 weeks
45 mins
No toxin control
Toxin only control
No virus control
AiE0450h-SYFP2
CMV-AADC-HA
AiE0450h-AADC-HA

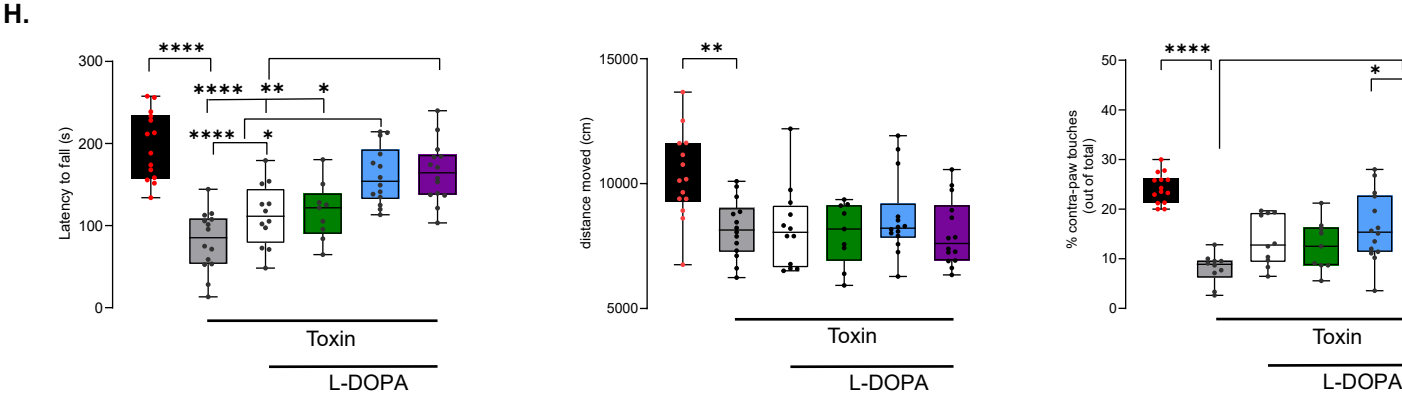
H.
Latency to fall (s)
distance moved (cm)
% contra-paw touches (out of total)
Toxin
L-DOPA

Figure 4

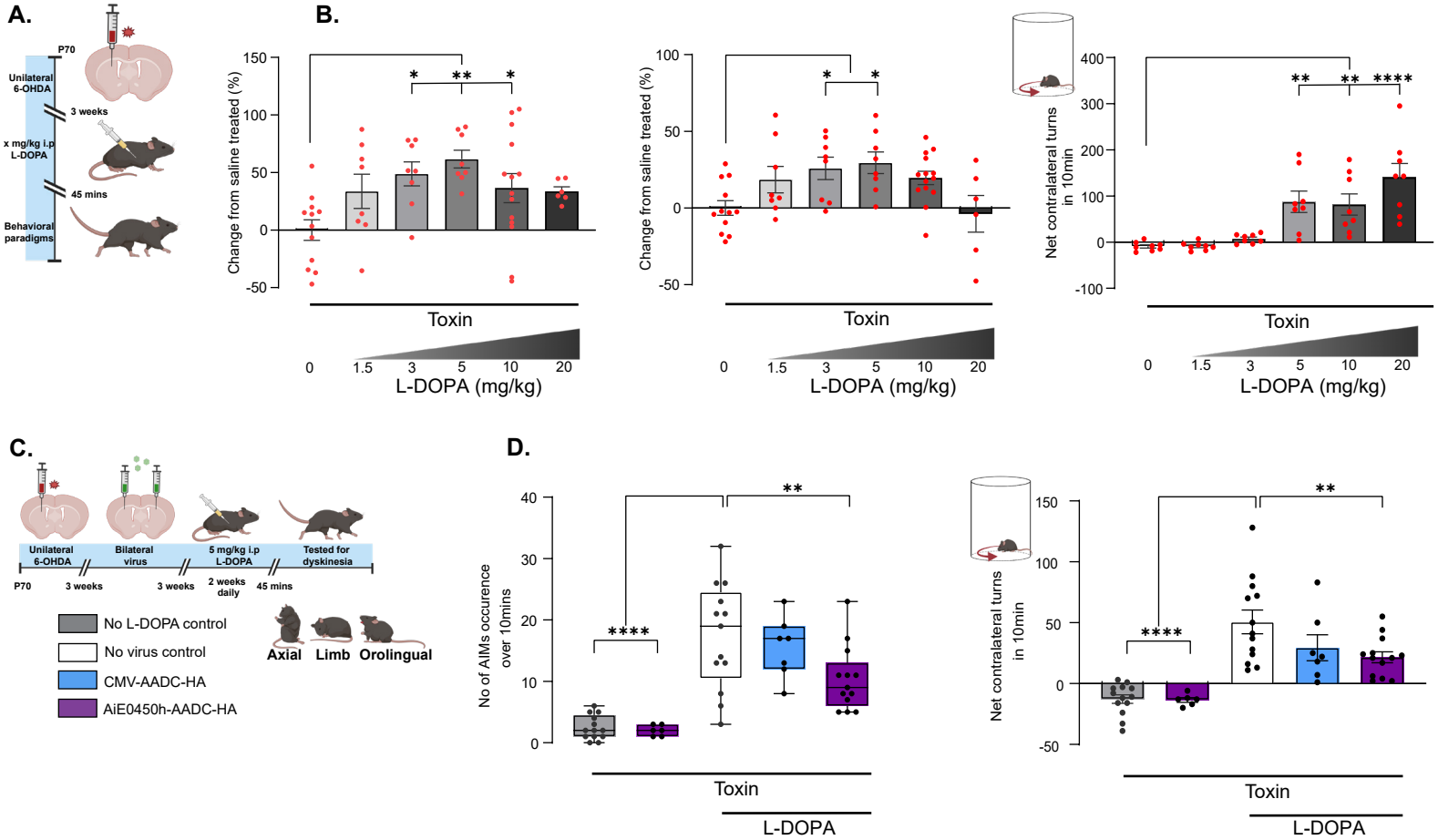
A.
P70
Unilateral 6-OHDA
3 weeks
x mg/kg i.p L-DOPA
45 mins
Behavioral paradigms
B.
Change from saline treated (%)
Toxin
L-DOPA (mg/kg)
0
1.5
3
5
10
20
Net contralateral turns in 10min
C.
Unilateral 6-OHDA
Bilateral virus
5 mg/kg i.p L-DOPA
Tested for dyskinesia
P70
3 weeks
3 weeks
2 weeks daily
45 mins
No L-DOPA control
No virus control
CMV-AADC-HA
AiE0450h-AADC-HA
Axial
Limb
Orolingual
D.
No of AIMs occurence over 10mins
Toxin
L-DOPA

Figure 5

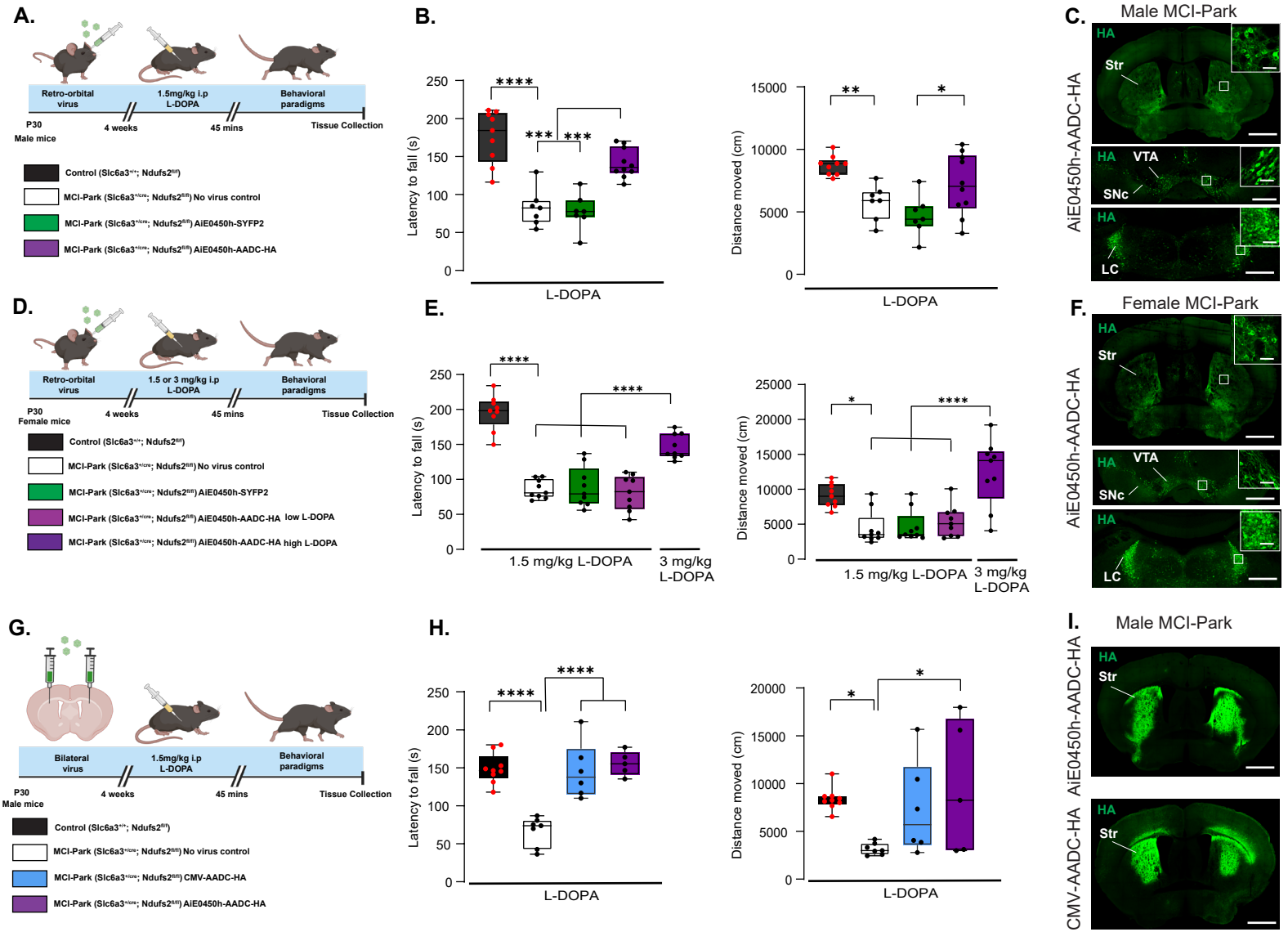
A.
Retro-orbital virus
1.5mg/kg i.p L-DOPA
Behavioral paradigms
P30 Male mice
4 weeks
45 mins
Tissue Collection
Control (Slc6a3+/+; Ndufs2fl/fl)
MCI-Park (Slc6a3+/cre; Ndufs2fl/fl) No virus control
MCI-Park (Slc6a3+/cre; Ndufs2fl/fl) AiE0450h-SYFP2
MCI-Park (Slc6a3+/cre; Ndufs2fl/fl) AiE0450h-AADC-HA
B.
Latency to fall (s)
L-DOPA
Distance moved (cm)
L-DOPA
C.
Male MCI-Park
AiE0450h-AADC-HA
HA
Str
VTA
SNc
LC
D.
Retro-orbital virus
1.5 or 3 mg/kg i.p L-DOPA
Behavioral paradigms
P30 Female mice
4 weeks
45 mins
Tissue Collection
Control (Slc6a3+/+; Ndufs2fl/fl)
MCI-Park (Slc6a3+/cre; Ndufs2fl/fl) No virus control
MCI-Park (Slc6a3+/cre; Ndufs2fl/fl) AiE0450h-SYFP2
MCI-Park (Slc6a3+/cre; Ndufs2fl/fl) AiE0450h-AADC-HA low L-DOPA
MCI-Park (Slc6a3+/cre; Ndufs2fl/fl) AiE0450h-AADC-HA high L-DOPA
E.
Latency to fall (s)
1.5 mg/kg L-DOPA
3 mg/kg L-DOPA
Distance moved (cm)
1.5 mg/kg L-DOPA
3 mg/kg L-DOPA
F.
Female MCI-Park
AiE0450h-AADC-HA
HA
Str
VTA
SNc
LC
G.
Bilateral virus
1.5mg/kg i.p L-DOPA
Behavioral paradigms
P30 Male mice
4 weeks
45 mins
Tissue Collection
Control (Slc6a3+/+; Ndufs2fl/fl)
MCI-Park (Slc6a3+/cre; Ndufs2fl/fl) No virus control
MCI-Park (Slc6a3+/cre; Ndufs2fl/fl) CMV-AADC-HA
MCI-Park (Slc6a3+/cre; Ndufs2fl/fl) AiE0450h-AADC-HA
H.
Latency to fall (s)
L-DOPA
Distance moved (cm)
L-DOPA
I.
Male MCI-Park
AiE0450h-AADC-HA
CMV-AADC-HA
HA
Str

Figure 6

A.

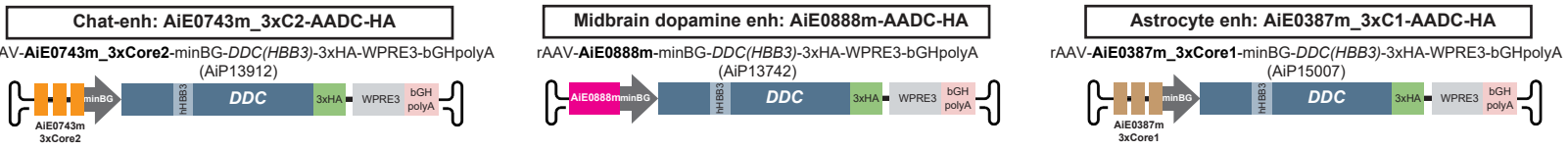

B. AiE0743m_3xC2-AADC-HA

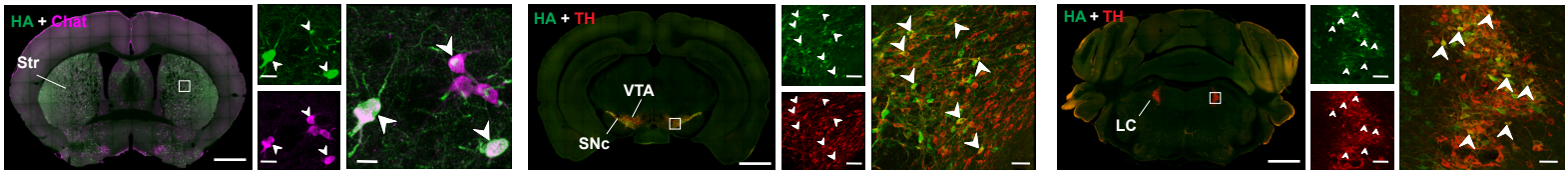

C. AiE0888m-AADC-HA

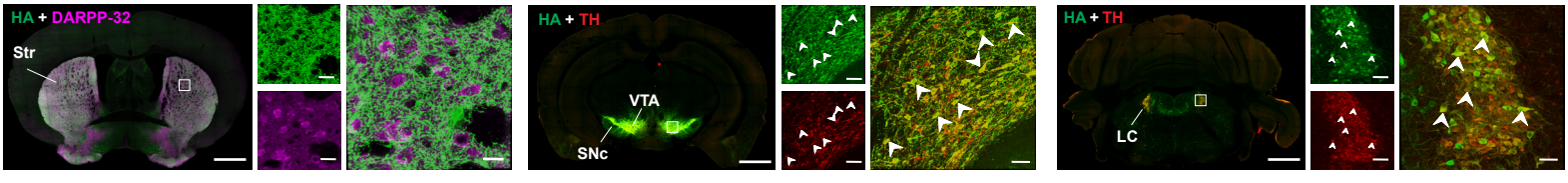

D. AiE0387m_3xC1-AADC-HA

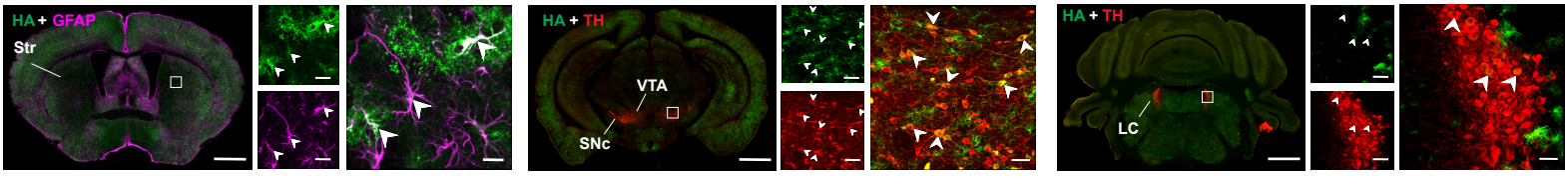

E.

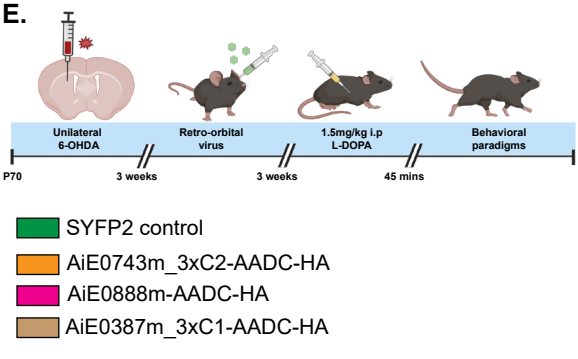

F.

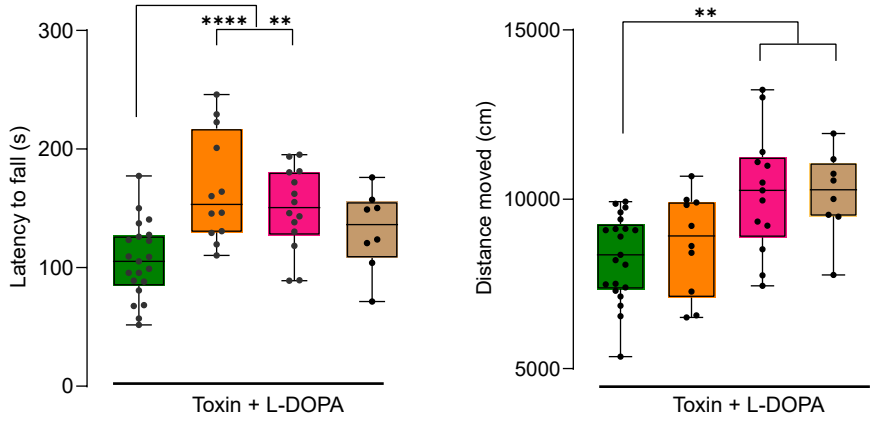

G.

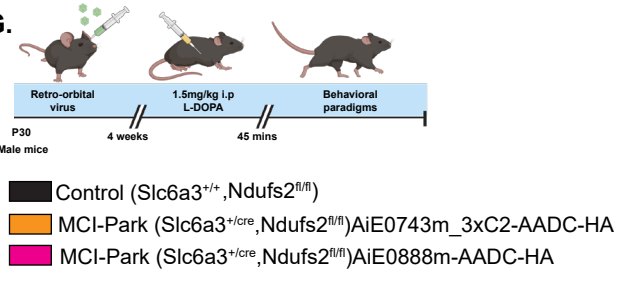

H.

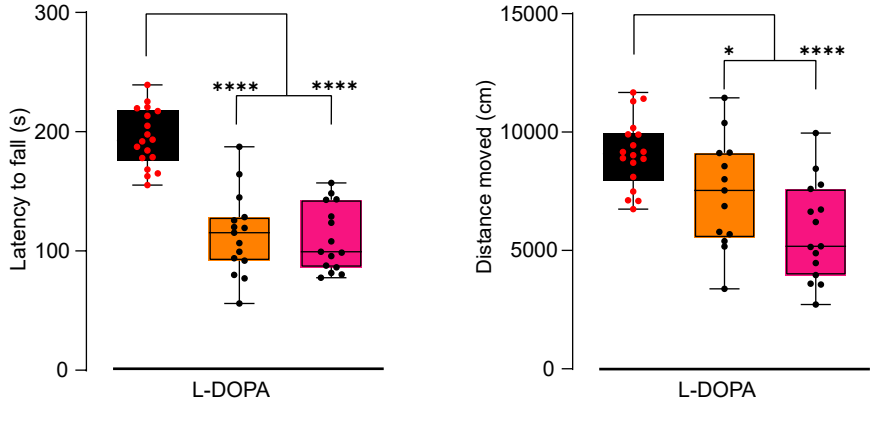

Figure 7

A. ICV: AiE0450h-AADC-HA

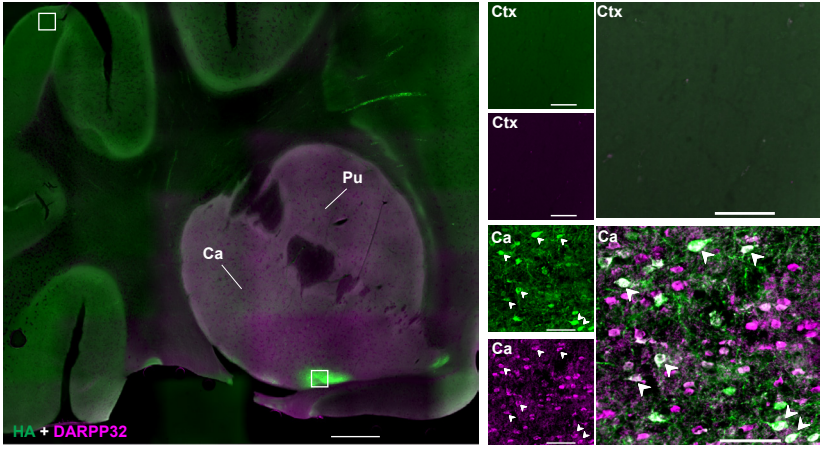

B. ICV: hSYN1-SYFP2-H2B

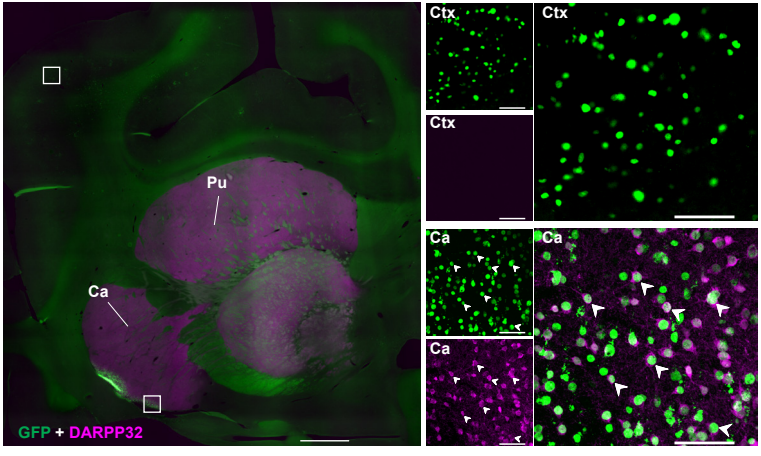

C. Intraparenchymal: AiE0450h-AADC-HA

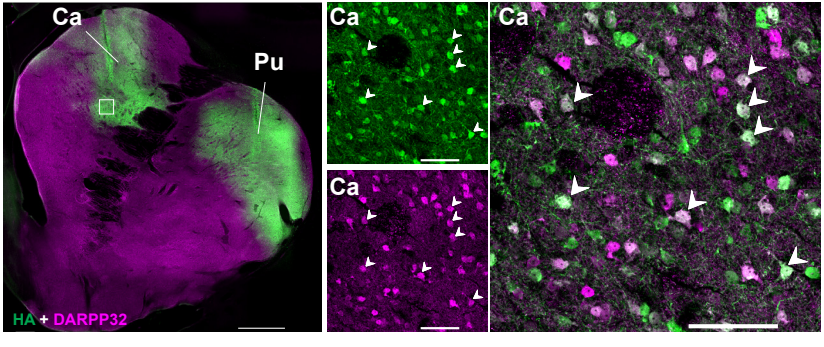

D. Specificity
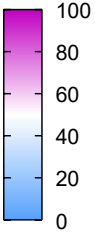
	ICV	IP
AiE0450h-AADC-HA	95.23	81.06
hSyn1-SYFP2-H2B	70.85	NA